May 1992

Design and Control of an In-Parallel Pneumatically-Actuated Manipulator

Thomas G. Sugar
University of Pennsylvania

University of Pennsylvania Department of Computer and Information Science Technical Report No. MS-CIS-92-63.

Design and Control of an In-Parallel Pneumatically-Actuated Manipulator

Abstract

The design and control of an in-parallel, pneumatically actuated manipulator is presented. In-parallel manipulators offer superior dynamic characteristics because of their high stiffness, low inertia, and potential for direct drive actuation. In this thesis, the three degree of freedom tripod manipulator is studied. The three degrees of freedom of the manipulator are exactly those that are required for force control perpendicular to a surface. These degrees of freedom are translations along the approach direction and rotations about the axes perpendicular to the approach direction. This body of research can be grouped into three parts. First the area of force control is examined with two purposes in mind, improving pneumatic force control, and understanding how force control has been traditionally implemented and the reasons for its limitations. Next, the improvement of the response of the mechanism and the implementation of different force control schemes are investigated. To improve the response of the system, shorter transmission lengths and an inner pressure feedback loop are added. Position control, force control, stiffness/compliance control, and impedance control, are all investigated, Lastly, a discussion of the advantages and possible uses of this mechanism is presented. The advantage of the parallel mechanism is the ability to regulate the force perpendicular to the surface. Thus, the mechanism can control the force perpendicular to the surface, while an arm attached to the mechanism can control the position of the end effector. This mechanism thus allows the hybrid position and force control problem to be decoupled. Obvious uses for applying a force perpendicular to a surface are tasks such as deburring or polishing. Another possible use could be peg insertion; a new design for peg insertion will be discussed. Lastly, this mechanism could be used as an ankle for a walking machine or a writ for a serial robot. The mechanism can adjust for unforeseen impacts and allow the system to be used in an unstructured environment.

Comments

University of Pennsylvania Department of Computer and Information Science Technical Report No. MS-CIS-92-63.

Design and Control Of An In-Parallel Pneumatically-Actuated Manipulator

MS-CIS-92-63
GRASP LAB 327

Thomas G. Sugar

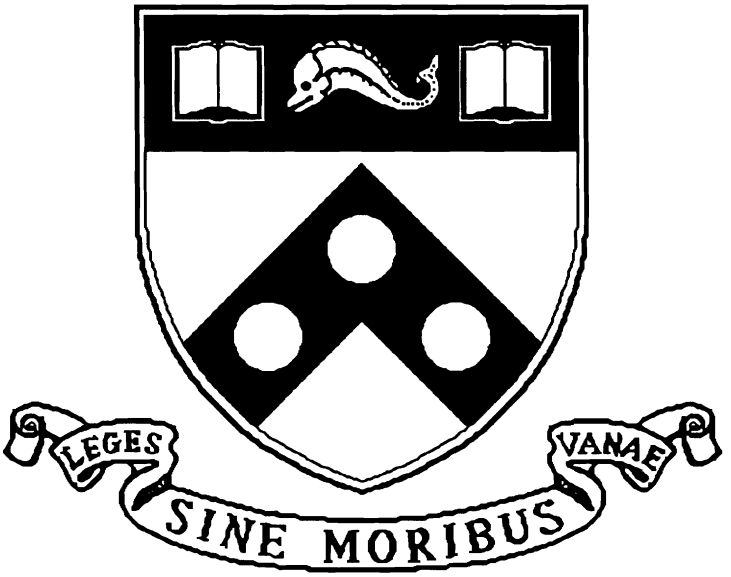

University of Pennsylvania
School of Engineering and Applied Science
Computer and Information Science Department
Philadelphia, PA 19104-6389

July 1992

UNIVERSITY OF PENNSYLVANIA
SCHOOL OF ENGINEERING AND APPLIED SCIENCE

Design and Control of an In-Parallel Pneumatically-Actuated Manipulator

Thomas G. Sugar

Philadelphia, Pennsylvania
May 1992

Abstract

The design and control of an in-parallel, pneumatically actuated manipulator is presented. In-parallel manipulators offer superior dynamic characteristics because of their high stiffness, low inertia, and potential for direct drive actuation. In this thesis, the three degree of freedom tripod manipulator is studied. The three degrees of freedom of the manipulator are exactly those that are required for force control perpendicular to a surface. These degrees of freedom are translations along the approach direction and rotations about the axes perpendicular to the approach direction. This body of research can be grouped into three parts. First the area of force control is examined with two purposes in mind, improving pneumatic force control, and understanding how force control has been traditionally implemented and the reasons for its limitations. Next, the improvement of the response of the mechanism and the implementation of different force control schemes are investigated. To improve the response of the system, shorter transmission lengths and an inner pressure feedback loop are added. Position control, force control, stiffness/compliance control, and impedance control, are all investigated. Lastly, a discussion of the advantages and possible uses of this mechanism is presented. The advantage of the parallel mechanism is the ability to regulate the force perpendicular to the surface. Thus, the mechanism can control the force perpendicular to the surface, while an arm attached to the mechanism can control the position of the end effector. This mechanism thus allows the hybrid position and force control problem to be decoupled. Obvious uses for applying a force perpendicular to a surface are tasks such as deburring or polishing. Another possible use could be peg insertion; a new design for peg insertion will be discussed. Lastly, this mechanism could be used as an ankle for a walking machine or a wrist for a serial robot. The mechanism can adjust for unforeseen impacts and allow the system to be used in an unstructured environment.

ACKNOWLEDGEMENTS

This research would not have been possible without the guidance and support of Dr. Vijay Kumar. Our weekly, and many times daily, discussions helped to further my research and broaden my interest in engineering.

The daily conversations, not always about engineering, with Chris Gerdes and Eric Paljug will be remembered. Many late nights were spent discussing music, political views, and business ideas. I cannot forget all of the electrical engineering and LaTeX help given to me by Mario Campos.

I would also like to mention the GRASP lab which has a unique friendly atmosphere. I enjoyed working with and learning from engineers whose backgrounds were widely different. The lab's computer and experimental support was greatly appreciated also.

From the GRASP lab I would like to thank Tarek Sobh, Julie Adams, Marcos Salganicoff, Tom Lindsay, Matthew Stein, Luca Bogoni, Stamps Howard, Filip Fuma, John Bradley for all of their help. I would also like to thank Gerda Kamberova, Chau-Chang Wang, Michael Chan, and Nilanjan Sarkar for their help as well.

A special thanks goes to George Pfreundschuh who laid the foundation for my work with the tripod manipulator.

I cannot forget to mention the help of both Bob Miller and Scott Doyle. Scott's skill at understanding motor controllers and Bob's machining advice helped me through some tough problems.

Contents

List of Tables

List of Figures

Chapter 1

Introduction

1.1 Objectives and Scope

The design and control of an in-parallel, pneumatically actuated manipulator is presented. In-parallel manipulators offer superior dynamic characteristics because of their high stiffness, low inertia, and potential for direct drive actuation [11]. Because of the compliance intrinsic to pneumatics, a pneumatically-actuated tripod manipulator has foreseen benefits which are twofold. One advantage is its ability to withstand large impacts, and the second is its ability to actively change its compliance. With these two advantages, the tripod manipulator can be used as an active compliant end effector which can absorb energy from unforeseen impacts.

The objectives of this research are:

- To study the dynamics of the tripod mechanism in order to develop control schemes for coordinating the multiple degrees of freedom.
- To investigate fundamental problems underlying force control. An important aspect of this is to develop models for pneumatic actuators to optimize the servo-level control.
- To develop different control schemes for the tripod mechanism including stiffness /compliance control, impedance control, and force control.

Before the manipulator can be controlled, the kinematics of the mechanism must be understood. The inverse and direct kinematics have been solved previously [25] and from the

this work, the stiffness and compliance matrices for the system are defined. An important feature of the manipulator is that it can only translate in the approach direction and rotate about the axes perpendicular to the approach direction. Similarly, we can control the force in the approach direction as well as the moments about the axes perpendicular to the approach direction. The forces along the axes perpendicular to the approach direction and the moment about the approach direction cannot be controlled, but are resisted.

The area of force control is examined with two purposes in mind: improving pneumatic force control, and understanding how force control has been traditionally implemented and the reasons for its limitations. Ideas to improve force control with pneumatic actuators have been examined with the aid of a one degree-of-freedom high performance testbed. The test bed employs small transmission lengths, graphite glass actuators, and an inner pressure feedback loop.

The implementation of force control is also studied using the one degree of freedom testbed. The force control model usually employs rigid body dynamics which algebraically relate the input to the output forces. Because the dynamics have not been modeled, the actuators at best can compensate for the forces in a static manner. The acausal system is studied using the one degree of freedom testbed and a controller based on discrete control laws. First, the importance of the difference rule applied when deriving the control law is studied. Secondly, the proportional and integral gains chosen are shown to be very important because these gains will change the overall behavior of the system.

Some of the ideas from the one degree of freedom testbed have been implemented in the mechanism. To improve the response of the system, shorter transmission lengths and an inner pressure feedback loop are added. Various force control methods which are applied to the mechanism are: stiffness/compliance control, impedance control, and force control. The stiffness of the system can be actively changed so that its response to various forces can be radically different. The impedance of the system can also be changed so that again the response of the mechanism to a certain force could be stiff, soft, overdamped or underdamped. The three degrees of freedom of the manipulator are exactly those that are required for force control along a surface. These degrees of freedom are translations along the approach direction and rotations about the axes perpendicular to the approach

direction. Thus, the mechanism could control the force along the surface, while an arm attached to the mechanism could control the position of the end effector. This mechanism thus allows the hybrid position and force control problem to be decoupled.

Finally, a discussion of the possible uses of this mechanism will be included. One possible use could be peg insertion; a new design for peg insertion will be discussed. Other obvious uses are applying a force along a surface which is needed in such tasks as deburring or polishing. Lastly, this mechanism could be used as an ankle for a walking machine or a wrist for a serial robot. The mechanism can adjust for unforeseen impacts and allow the system to be used in an unstructured environment.

1.2 Literature Review

1.2.1 In-parallel Manipulation - Tripod Mechanism

The kinematics of a tripod mechanism have been studied by Lee and Shah [14] Waldron and Roth [34] Pfreundschuh et. al. [25] [32] and others. In Pfreundschuh's master thesis [25], the kinematics of the mechanism are thoroughly described including the formulation of the Jacobian and its inverse. He also describes the design parameters needed for building a direct drive, pneumatically actuated manipulator. Because of the large force to weight ratio of the actuators, Shah [13] describes a small manipulator which can move large objects. Also because the actuators directly drive the system and air is naturally compliant, the mechanism can also achieve high performance force control.

1.2.2 Pneumatic Actuation Systems in Robotics

Pneumatic systems have many advantages to electric motor or hydraulic systems which include large output to weight ratios, low cost, and cleanliness. A major drawback to pneumatic systems has been the low bandwidth caused mainly by the transport lag due to the compliance of air. Both Bobrow [1] and Mannetje [16] have included an inner pressure feedback loop which increased the position control bandwidth of the system. When the additional pressure feedback is included, Bobrow showed the root loci of the system are shifted to the left, thus improving the performance of the system.

1.2.3 Control Schemes Involving Stiffness/Compliance Control and Applications

Impedance control [39] tries to regulate the relationship between forces and velocities. The active impedance control method describes an algorithm for achieving a desired impedance resulting from an external force. In his book [39], Yoshikawa describes a one degree of freedom case for active impedance control. Essentially, one would like to control the desired mass, damping, and stiffness parameters of the system.

Stiffness or compliance control [39], is a subset of impedance control. If the desired mass and damping parameters of the system are equal to zero, only the stiffness parameter is left. With these parameters, only the stiffness is controlled for a given external force.

Both stiffness control and impedance control can actively change the compliance of the link. Passive impedance methods have also been researched [36]. Passive methods usually consist of a wrist which is designed with passive springs or some type of rubber material. A remote compliance center [39] is a passive mechanical device which creates a compliance center at the tip of the peg. Whitney [36] describes a passive remote compliance center which can insert rigid pegs. Drawbacks to passive devices include the inability to change the impedance parameters. Flexible manufacturing cannot be achieved if a new mechanical device needs to be built every time a new situation occurs. Our pneumatically controlled tripod mechanism can actively change its stiffness parameters. Because the stiffness parameters can be changed, this mechanism offers a better design for a wrist or an ankle in many situations.

Chapter 2

The Tripod Mechanism

2.1 Kinematics

The kinematics follow directly from the work done by Pfreundschuh [25]. Only the kinematics needed to derive the stiffness matrix are presented in detail. For a more extensive discussion, then refer to the previous work by Pfreundschuh.

2.1.1 Mechanism Description

The structure of the system is shown in Figure 2.1. Three prismatic links are attached to a lower base frame and an upper platform. The prismatic joints are attached to the base frame with pin joints and are attached to the upper platform with ball joints. Each link has five degrees of freedom, three degrees from the ball joint, one degree from the extension of the link, and one degree from the pin joint.

2.1.2 Rotation Matrix

The inverse kinematics are discussed briefly in order for the reader to better understand the manipulator. For this mechanism, the inverse kinematics are much easier to solve than the direct kinematics. First an arbitrary rotation about the top platform will be discussed.

The upper platform coordinate system will be referred to as **xyz** and the fixed base coordinate system will be referred to as **XYZ** as shown in Figure 2.1. A coordinate frame is fixed to the upper platform which defines the **z** axis normal to the moving platform.

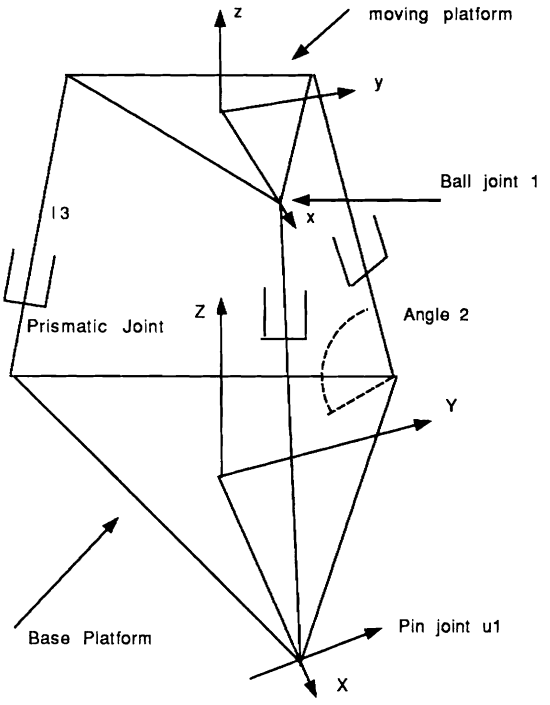

Figure 2.1: Coordinate Systems

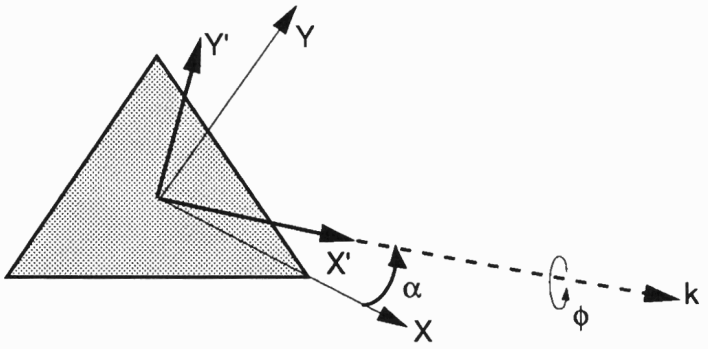

Figure 2.2: Rotation of the Upper Platform

The goal is then to describe a vector in the moving coordinate system by a vector in a fixed coordinate system. Because of the kinematic constraints, only two angles α and ϕ are needed to describe a rotation of the upper platform. The arbitrary rotation in the **xy** plane can be described by some rotation ϕ about an axis $\hat{k}$ see Figure 2.2. The angle α describes the position of the $\hat{k}$ axis in the **xy** plane. Note, the upper platform actually moves relative to the **X**, **Y**, and **Z** directions because of the coupling of the links with the revolute joints. The platform coordinate frame will actually move slightly, but the movement can be described by the angles, α and ϕ.

A rotation matrix can be described easily for this type of motion. To move from the fixed coordinate frame to the new coordinate frame, the fixed frame is first rotated about the **z** axis until the **x** axis coincides with the $\hat{k}$ axis. Then the frame is rotated about its **x** axis ϕ degrees. Finally, the **xy** axes are repositioned to their original locations by rotating about the **z** axis minus α degrees.

A vector **r** in the moving frame can then be described by a vector **p** in a fixed **xyz** frame by a series of rotations. Note, the upper platform frame actually moves slightly; the actual deflection of the frame occurs because the rotation of the upper platform is not pure.

$$\mathbf{p} = [\Pi][R_\phi][\Pi^{-1}]\mathbf{r} \tag{2.1}$$

where R_ϕ describes the rotation ϕ about $\hat{k}$ and Π describes the rotation α about the **z** axis.

The combined rotation matrix R can easily be found.

$$[R] = \begin{bmatrix} k_x^2 + k_y^2 C\phi & k_x k_y(1 - C\phi) & k_y S\phi \\ k_x k_y(1 - C\phi) & k_y^2 + k_x^2 C\phi & -k_x S\phi \\ -k_y S\phi & k_x S\phi & C\phi \end{bmatrix} \tag{2.2}$$

where

$$k_x = C\alpha \tag{2.3}$$

$$k_y = S\alpha \tag{2.4}$$

The angle ϕ is limited to less than π degrees because the physical platform cannot rotate through itself.

$$-\pi \leq \alpha < \pi \tag{2.5}$$

$$0 \leq \phi < \pi \tag{2.6}$$

2.1.3 Transformation Matrix

The translation from the base coordinate system to the upper platform coordinate system still needs to be described. The vector from the base to the upper platform can be described by three parameters X_c, Y_c, and Z_c. These three parameters describe the actual translation of the upper platform. Because only three generalized coordinates are needed to describe the platform, two of the five parameters, X_c, Y_c, Z_c, α, and ϕ, are dependent. Two extra constraints on the mechanism are needed to eliminate the extra coordinates. The constraints follow from the fact that the revolute joints at the base of the platform only have one degree of freedom. From the revolute joint constraints on the links, X_c and Y_c are related to α and ϕ.

$$X_c = \frac{1}{2}\rho(1 - C_\phi)C_{2\alpha} \tag{2.7}$$

$$Y_c = -\frac{1}{2}\rho(1 - C_\phi)S_{2\alpha} \tag{2.8}$$

where

$$\rho = \frac{r}{R} \qquad X_c = \frac{x_c}{R} \qquad Y_c = \frac{y_c}{R} \qquad Z_c = \frac{z_c}{R}$$

A third constraint can also be derived from the fact that the links cannot translate in a parallel direction to the revolute joints. The constraint follows from the homogeneous transformation described below.

$$[T] = \begin{bmatrix} n_1 & o_1 & a_1 & x_c \\ n_2 & o_2 & a_2 & y_c \\ n_3 & o_3 & a_3 & z_c \\ 0 & 0 & 0 & 1 \end{bmatrix} \tag{2.9}$$

The last constraint requires that:

$$n_2 = o_1 \tag{2.10}$$

From this constraint, it can be shown that the system cannot produce a *pure rotation* about the **z** axis. Physically the platform cannot produce a rotation about the **Z** axis independent from other motions. The constraint does not mean that a rotation in the **Z** axis cannot occur. A rotation in the **Z** axis can occur but the rotation is coupled with a rotation in another arbitrary axis. In the discussion of forward kinematics, it will be shown that an angular velocity about the **Z** axis is nonzero which must mean that there is a rotation about the **Z** axis.

The transformation matrix can then be described as

$$[T] = \begin{bmatrix} k_x^2 + k_y^2 C\phi & k_x k_y (1 - C\phi) & k_y S\phi & x_c \\ k_x k_y (1 - C\phi) & k_y^2 + k_x^2 C\phi & -k_x S\phi & y_c \\ -k_y S\phi & k_x S\phi & C\phi & z_c \\ 0 & 0 & 0 & 1 \end{bmatrix} \tag{2.11}$$

To summarize:

- ϕ and α describe the upper platform's rotation.
- x_c, y_c, and z_c describe the translation of the upper platform.
- The upper platform exhibits small translations in the **X Y** directions as well as a slight rotation about the **Z** axis.

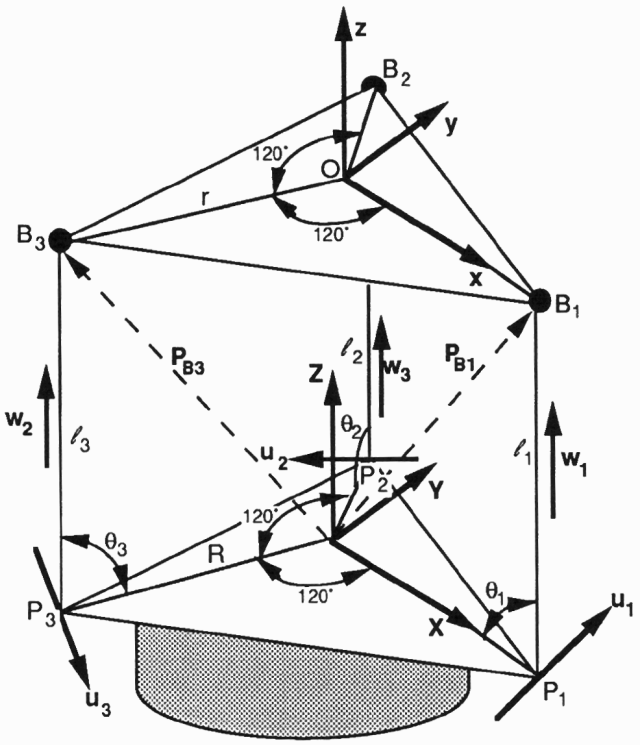

Figure 2.3: Diagram of the Upper and Lower Platform

2.1.4 Direct Kinematics

As stated before, the inverse kinematic analysis is much easier to solve than the direct kinematic analysis. A detailed diagram of the vectors needed for the kinematic analysis is shown in Figure 2.3. The generalized coordinates for this analysis include θ_1, θ_2, θ_3, and l_1, l_2, l_3. The scalar l_i describes the magnitude of the corresponding link while the angle θ_i corresponds to the direction of the link. Again, since there are only three degrees of freedom, the link lengths must be related to the link angles. Three equations can be derived, but they are nonlinear and must be solved using a numerical analysis program.

To begin the derivation, the vector $\mathbf{p}$ is defined as the location of the ball joint in base coordinates as shown in Figure 2.3. If two adjacent vectors $\mathbf{p_i}$ are subtracted, the magnitude must equal $\sqrt{3}r$. For example,

$$\|\mathbf{p_1} - \mathbf{p_2}\|$$

describes the distance between the two links. This distance is exactly the length of one side

of the equilateral triangle.

$$\|\mathbf{p_1} - \mathbf{p_2}\| = \|\mathbf{p_1} - \mathbf{p_2}\| = \|\mathbf{p_3} - \mathbf{p_1}\| = \sqrt{3}r$$

From the defined coordinate system,

$$\mathbf{l_1} = l_1 \begin{pmatrix} -\cos\theta_1 \\ 0 \\ \sin\theta_1 \end{pmatrix} \quad \mathbf{l_2} = l_2 \begin{pmatrix} \frac{1}{2}\cos\theta_2 \\ -\frac{\sqrt{3}}{2}\cos\theta_2 \\ \sin\theta_2 \end{pmatrix} \quad \mathbf{l_3} = l_3 \begin{pmatrix} \frac{1}{2}\cos\theta_3 \\ \frac{\sqrt{3}}{2}\cos\theta_3 \\ \sin\theta_3 \end{pmatrix} \tag{2.12}$$

$$\mathbf{p_1} = \mathbf{l_1} + \begin{pmatrix} R \\ 0 \\ 0 \end{pmatrix} \quad \mathbf{p_2} = \mathbf{l_2} + \begin{pmatrix} -\frac{1}{2}R \\ \frac{\sqrt{3}}{2}R \\ 0 \end{pmatrix} \quad \mathbf{p_3} = \mathbf{l_3} + \begin{pmatrix} -\frac{1}{2}R \\ -\frac{\sqrt{3}}{2}R \\ 0 \end{pmatrix} \tag{2.13}$$

The constraint equations then become:

$$\begin{aligned} 0 &= l_1^2 + l_2^2 + 3R^2 - 3r^2 + l_1 l_2 \cos\theta_1 \cos\theta_2 - 2l_1 l_2 \sin\theta_1 \sin\theta_2 \\ &\quad -3l_1 \cos\theta_1 R - 3l_2 \cos\theta_2 R \end{aligned} \tag{2.14}$$

$$\begin{aligned} 0 &= l_2^2 + l_3^2 + 3R^2 - 3r^2 + l_2 l_3 \cos\theta_2 \cos\theta_3 - 2l_2 l_3 \sin\theta_2 \sin\theta_3 \\ &\quad -3l_2 \cos\theta_2 R - 3l_3 \cos\theta_3 R \end{aligned} \tag{2.15}$$

$$\begin{aligned} 0 &= l_3^2 + l_1^2 + 3R^2 - 3r^2 + l_3 l_1 \cos\theta_3 \cos\theta_1 - 2l_3 l_1 \sin\theta_3 \sin\theta_1 \\ &\quad -3l_3 \cos\theta_3 R - 3l_1 \cos\theta_1 R \end{aligned} \tag{2.16}$$

These three equations are solved using a Newton-Raphson routine. The link lengths are entered along with three estimates for the angles. Cramer's rule is used to determine the increment amount for each angle. Only a couple of iterations are needed to determine the angles which solve the equations for a defined minimum error.

2.1.5 Workspace for the Manipulator

The workspace for the manipulator is found using an iterative process. A computer program is written which calculates the link lengths and link angles for many different positions. At

each specified position of the upper platform, x_c, y_c, and z_c are found. The coordinates, x_c, y_c, and z_c are determined from the ball joint angles [14]. For our manipulator, $R = r = 3.5$ inches and z_c varies from three to five inches. The workspace for this geometry is shown in Figure 2.4.

2.1.6 The Jacobian Matrix

The Jacobian relates the described end effector velocities to the joint velocities. Because the mechanism only has three degrees of freedom, three more degrees of freedom are needed to form an inverse Jacobian which relates any arbitrary set of end effector velocities to a set of joint velocities. If only three joint velocities, namely the velocities of the actuators, are available, then only a subset of end effector velocities can possibly be obtained. To obtain the extra three degrees of freedom which forms an invertible Jacobian, Roth et. al. [33] propose to mount the tripod mechanism to a three degree of freedom wrist. Alternatively, the in-parallel three degree-of-freedom mechanism proposed by Kumar et. al. [11] could provide the three degrees of freedom.

Assuming that a three degree-of-freedom spherical wrist is employed, the inverse Jacobian can then be described as:

$$\begin{bmatrix} \dot{\mathbf{l}} \\ \dot{\Psi} \end{bmatrix} = \begin{bmatrix} \Gamma_c \\ \Gamma_r \end{bmatrix} \begin{bmatrix} \mathbf{v} \\ \omega \end{bmatrix} \tag{2.17}$$

where $\dot{\mathbf{l}}$ are the actuator velocities supplied by the mechanism and $\dot{\Psi}$ are the angular velocities supplied by the added wrist. Γ_c and Γ_r are both three by six matrices. If $\dot{\Psi} = 0$ because an extra wrist is not available, then Γ_c describes the available rotations or motions that are obtainable by the mechanism while satisfying the equation $\Gamma_r = 0$.

The inverse Jacobian is calculated by describing the velocity of the ball joints. Four sets of vectors need to be defined:

$\mathbf{p_i}$ - the vector from the base frame to the ball joint i

$\mathbf{w_i}$ - the unit vector describing the direction of link i

$\mathbf{u_i}$ - the unit vector along the axis of pin joint i

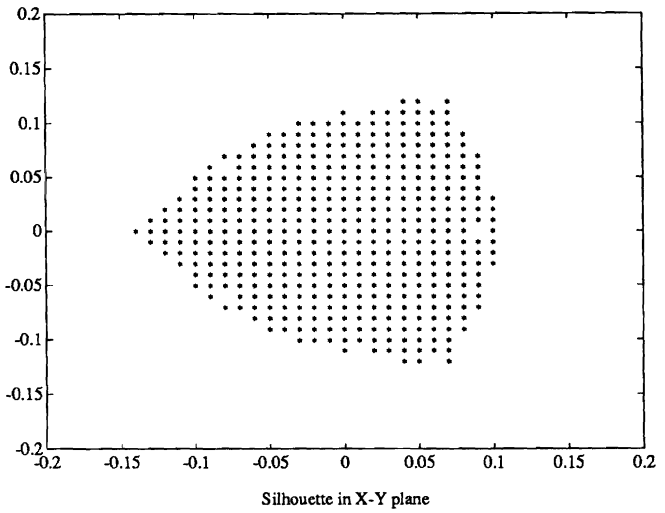

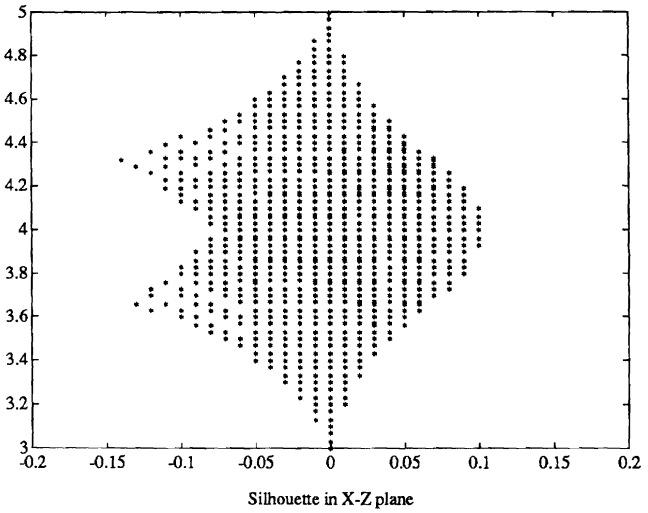

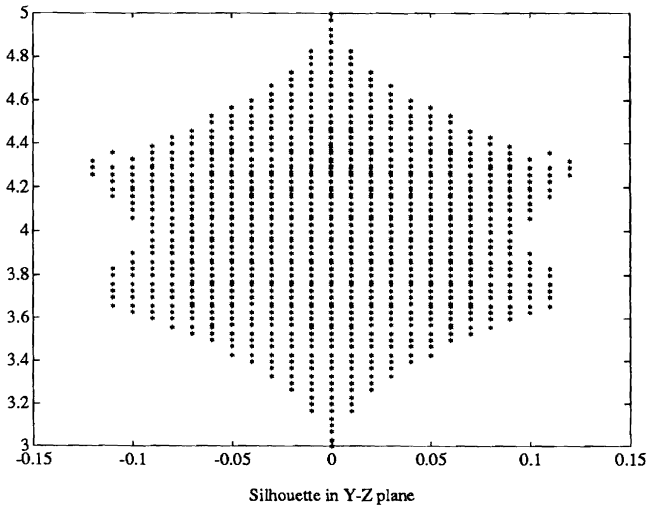

Figure 2.4: Manipulator Workspace

$\mathbf{q_i}$ - the vector from the origin of the upper platform frame to the ball joint i

All vectors are described in the base **XYZ** frame; therefore the end effector velocities are described in the base frame also.

$$\mathbf{p_1} = \begin{pmatrix} -l_1\cos\theta_1 + R \\ 0 \\ l_1\sin\theta_1 \end{pmatrix} \quad \mathbf{p_2} = \begin{pmatrix} \frac{1}{2}l_2\cos\theta_2 - \frac{1}{2}R \\ -\frac{\sqrt{3}}{2}l_2\cos\theta_2 + \frac{\sqrt{3}}{2}R \\ l_2\sin\theta_2 \end{pmatrix} \quad \mathbf{p_3} = \begin{pmatrix} \frac{1}{2}l_3\cos\theta_3 - \frac{1}{2}R \\ \frac{\sqrt{3}}{2}l_3\cos\theta_3 - \frac{\sqrt{3}}{2}R \\ l_3\sin\theta_3 \end{pmatrix} \tag{2.18}$$

$$\mathbf{w_1} = \begin{pmatrix} \cos\theta_1 \\ 0 \\ \sin\theta_1 \end{pmatrix} \quad \mathbf{w_2} = \begin{pmatrix} \frac{1}{2}\cos\theta_2 \\ -\frac{\sqrt{3}}{2}\cos\theta_2 \\ \sin\theta_2 \end{pmatrix} \quad \mathbf{w_3} = \begin{pmatrix} \frac{1}{2}\cos\theta_3 \\ \frac{\sqrt{3}}{2}\cos\theta_3 \\ \sin\theta_3 \end{pmatrix} \tag{2.19}$$

$$\mathbf{u_1} = \begin{pmatrix} 0 \\ 1 \\ 0 \end{pmatrix} \quad \mathbf{u_2} = \begin{pmatrix} -\frac{\sqrt{3}}{2} \\ -\frac{1}{2} \\ 0 \end{pmatrix} \quad \mathbf{u_3} = \begin{pmatrix} \frac{\sqrt{3}}{2} \\ -\frac{1}{2} \\ 0 \end{pmatrix} \tag{2.20}$$

The vectors $\mathbf{q_i}$ are defined as the vectors $\mathbf{p_i}$ minus the vector from the origin of the base coordinate frame to the origin of the upper platform frame.

$$\mathbf{q_1} = \begin{pmatrix} -l_1\cos\theta_1 + R - x_c \\ -y_c \\ l_1\sin\theta_1 - z_c \end{pmatrix} \quad \mathbf{q_2} = \begin{pmatrix} \frac{1}{2}l_2\cos\theta_2 - \frac{1}{2}R - x_c \\ -\frac{\sqrt{3}}{2}l_2\cos\theta_2 + \frac{\sqrt{3}}{2}R - y_c \\ l_2\sin\theta_2 - z_c \end{pmatrix} \quad \mathbf{q_3} = \begin{pmatrix} \frac{1}{2}l_3\cos\theta_3 - \frac{1}{2}R - x_c \\ \frac{\sqrt{3}}{2}l_3\cos\theta_3 - \frac{\sqrt{3}}{2}R - y_c \\ l_3\sin\theta_3 - z_c \end{pmatrix} \tag{2.21}$$

The velocity of the ball joint is the divergence of the vector $\mathbf{p}$ plus the additional term caused by the angular velocity, $\dot{\Psi}$, of the wrist. The velocity of the ball joint can then be defined.

$$\mathbf{v_{Bi}} = \dot{\Psi} \times \mathbf{p_{Bi}} + \dot{\mathbf{p}}_{\mathbf{Bi}} \tag{2.22}$$

where

$$\dot{\mathbf{p}}_{\mathbf{Bi}} = \dot{\mathbf{l}}_{\mathbf{i}}\mathbf{w_i} + l_i\mathbf{w_i}\dot{\theta}_i \tag{2.23}$$

or

$$\dot{\mathbf{p}}_{\mathbf{Bi}} = \dot{\mathbf{l}}_{\mathbf{i}}\mathbf{w_i} + (\mathbf{u_i} \times l_i\mathbf{w_i})\,\dot{\theta}_i \tag{2.24}$$

The velocity of the ball joint can also be written in terms of the end effector velocity, $\mathbf{v}$ and ω.

$$\mathbf{v_{Bi}} = \mathbf{v} + \omega \times \mathbf{q_i} \tag{2.25}$$

By setting Equations (2.22) and (2.25) equal, the joint velocities $\dot{\mathbf{l}}$ and $\dot{\Psi}$ can be found after some manipulation.

$$\dot{\mathbf{l}} = [\gamma_{lv} - A\,\gamma_{21}]\mathbf{v} + [\gamma_{l\omega} - A\,\gamma_{22}]\omega \tag{2.26}$$

$$\dot{\Psi} = \gamma_{21}\mathbf{v} + \gamma_{22}\omega \tag{2.27}$$

where

$$\gamma_{lv} = \begin{bmatrix} \mathbf{w}_1^T \\ \mathbf{w}_2^T \\ \mathbf{w}_3^T \end{bmatrix} \qquad \gamma_{l\omega} = \begin{bmatrix} [\mathbf{q}_1 \times \mathbf{w}_1]^T \\ [\mathbf{q}_2 \times \mathbf{w}_2]^T \\ [\mathbf{q}_3 \times \mathbf{w}_3]^T \end{bmatrix} \qquad A = \begin{bmatrix} [\mathbf{p}_1 \times \mathbf{w}_1]^T \\ [\mathbf{p}_2 \times \mathbf{w}_2]^T \\ [\mathbf{p}_3 \times \mathbf{w}_3]^T \end{bmatrix}$$

$$\gamma_{21} = \begin{bmatrix} [\mathbf{p}_1 \times \mathbf{u}_1]^T \\ [\mathbf{p}_2 \times \mathbf{u}_2]^T \\ [\mathbf{p}_3 \times \mathbf{u}_3]^T \end{bmatrix}^{-1} \begin{bmatrix} \mathbf{u}_1^T \\ \mathbf{u}_2^T \\ \mathbf{u}_3^T \end{bmatrix} \qquad \gamma_{22} = \begin{bmatrix} [\mathbf{p}_1 \times \mathbf{u}_1]^T \\ [\mathbf{p}_2 \times \mathbf{u}_2]^T \\ [\mathbf{p}_3 \times \mathbf{u}_3]^T \end{bmatrix}^{-1} \begin{bmatrix} [\mathbf{q}_1 \times \mathbf{u}_1]^T \\ [\mathbf{q}_2 \times \mathbf{u}_2]^T \\ [\mathbf{q}_3 \times \mathbf{u}_3]^T \end{bmatrix}$$

The inverse Jacobian follows directly from these equations.

$$\begin{bmatrix} \dot{\mathbf{l}} \\ \dot{\Psi} \end{bmatrix} = \left[\begin{array}{c|c} \gamma_{lv} - A\,\gamma_{21} & \gamma_{l\omega} - A\,\gamma_{22} \\ \hline \gamma_{21} & \gamma_{22} \end{array}\right] \begin{bmatrix} \mathbf{v} \\ \omega \end{bmatrix} \tag{2.28}$$

The inverse Jacobian relates the desired end effector velocities with the joint velocities. The direction of the desired end effector velocities are expressed with respect to the fixed base frame. Since the Jacobian is just the inverse of J^{-1}, it can be found easily by inverting the matrix.

2.1.7 The Simplified Inverse Jacobian for the Tripod Manipulator

The inverse Jacobian can be simplified by setting $\dot{\Psi} = 0$. From Equation (2.27)

$$\gamma_{21}\mathbf{v} = -\gamma_{22}\omega \tag{2.29}$$

and

$$\begin{bmatrix} \dot{\mathbf{i}} \end{bmatrix} = \begin{bmatrix} \gamma_{lv} & | & \gamma_{l\omega} \end{bmatrix} \begin{bmatrix} \mathbf{v} \\ \omega \end{bmatrix} \tag{2.30}$$

The set of simplified equations describes the set of rotations or motions that can be supplied by the tripod mechanism.

2.1.8 Forward Kinematics

The forward kinematics are solved using the same velocity equations above [25]. If $\dot{\Psi} = 0$, Pfreundschuh shows

$$\omega = [A_\omega] \begin{bmatrix} \dot{\mathbf{i}} \end{bmatrix} \tag{2.31}$$

$$\mathbf{v} = [A_v] \begin{bmatrix} \dot{\mathbf{i}} \end{bmatrix} \tag{2.32}$$

From these equations, A_ω describes end effector angular velocities from a given set of link velocities. In general, a set of link velocities will produce a velocity in the **X** and **Y** directions as well as an angular velocity in the **Z** direction. These velocities are described in the base coordinate frame **XYZ**. This result may seem counterintuitive because the mechanism should only have three degrees of freedom, but a velocity in the **X** direction can occur, for example, and is *coupled* with a rotation described by α and ϕ. Pure velocities in the **X** and **Y** directions and pure angular velocities in the **Z** direction cannot occur. Also, the movement in these directions is very small.

The only pure translation for the mechanism that exists is in the **Z** direction as long as the mechanism stays in the *home position.* If all angles are ninety degrees and the desired output is only a velocity in the **Z** direction, then the translation is pure. This is not the case if the platform is tilted. If it is tilted and the desired translation is in the **Z** direction, there will be a velocity in the **XY** frame. The angular rotations in the **X** and **Y** directions can be large, but the actual rotation is not pure because as the upper platform rotates, x_c and y_c change.

2.1.9 Force Decomposition based on the Simplified Inverse Jacobian

From the preceding analysis, the force decomposition which relates end effector forces to the joint forces can be derived. Using the duality principle:

$$\begin{bmatrix} \mathbf{R} \\ \mathbf{C} \end{bmatrix} = \left[\begin{array}{c|c} \Gamma_c^T & \Gamma_r^T \end{array}\right] \begin{bmatrix} \mathbf{F} \\ \tau \end{bmatrix} \tag{2.33}$$

where $\mathbf{R}$ describes the end effector forces in the base frame, $\mathbf{C}$ describes the end effector moments in the base frame, $\mathbf{F}$ are the forces produced by the links, and τ are the torques produced by the added spherical wrist. Again by restricting $\dot{\Psi} = 0$, the Jacobian is simplified.

$$\begin{bmatrix} \mathbf{R} \\ \mathbf{C} \end{bmatrix} = \begin{bmatrix} \Gamma_c^T \end{bmatrix} \begin{bmatrix} \mathbf{F} \end{bmatrix} = \begin{bmatrix} \gamma_{lv}^T \\ \gamma_{l\omega}^T \end{bmatrix} \begin{bmatrix} \mathbf{F} \end{bmatrix} \tag{2.34}$$

$$\begin{Bmatrix} R_X \\ R_Y \\ R_Z \\ C_X \\ C_Y \\ C_Z \end{Bmatrix} = \left[\begin{array}{c|c|c} \mathbf{w}_1 & \mathbf{w}_2 & \mathbf{w}_3 \\ \mathbf{q}_1 \times \mathbf{w}_1 & \mathbf{q}_2 \times \mathbf{w}_2 & \mathbf{q}_3 \times \mathbf{w}_3 \end{array}\right] \begin{Bmatrix} F_1 \\ F_2 \\ F_3 \end{Bmatrix} \tag{2.35}$$

A distinction between τ and $\dot{\Psi}$ must be made. $\dot{\Psi}$ is set to zero because the mechanism is not attached to a wrist and is restricted from moving. It is not the case that τ is equal to zero. Torques at the base of the platform do occur, but cannot be controlled. These torques are resisted unless the structure of the manipulator fatigues. The set of equations defined in (2.35) describe the end effector forces that can be controlled by the input forces to each link, $\mathbf{F}$. The set of end effector forces that can be controlled are only a subset of the possible end effector forces that can occur.

$$\begin{Bmatrix} R_X \\ R_Y \\ R_Z \\ C_X \\ C_Y \\ C_Z \end{Bmatrix} = \begin{bmatrix} -\cos\theta_1 & \frac{1}{2}\cos\theta_2 \\ 0 & -\frac{\sqrt{3}}{2}\cos\theta_2 \\ \sin\theta_1 & \sin\theta_2 \\ -y_c\sin\theta_1 & \frac{\sqrt{3}}{2}R\sin\theta_2 - y_c\sin\theta_2 - \frac{\sqrt{3}}{2}z_c\cos\theta_2 \\ -R\sin\theta_1 + x_c\sin\theta_1 + z_c\cos\theta_1 & \frac{1}{2}R\sin\theta_2 + x_c\sin\theta_2 - \frac{1}{2}z_c\cos\theta_2 \\ -y_c\cos\theta_1 & \frac{\sqrt{3}}{2}x_c\cos\theta_2 + \frac{1}{2}y_c\cos\theta_2 \end{bmatrix}$$

$$\begin{bmatrix} \frac{1}{2}\cos\theta_2 \\ \frac{\sqrt{3}}{2}\cos\theta_3 \\ \sin\theta_3 \\ -\frac{\sqrt{3}}{2}R\sin\theta_3 - y_c\sin\theta_3 + \frac{\sqrt{3}}{2}z_c\cos\theta_3 \\ \frac{1}{2}R\sin\theta_3 + x_c\sin\theta_3 - \frac{1}{2}z_c\cos\theta_3 \\ -\frac{\sqrt{3}}{2}x_c\cos\theta_3 + \frac{1}{2}y_c\cos\theta_3 \end{bmatrix} \begin{Bmatrix} F_1 \\ F_2 \\ F_3 \end{Bmatrix}$$

In the home position, only forces in the **Z**, and the moments about the **X** and **Y** directions can be controlled.

$$\begin{Bmatrix} R_X \\ R_Y \\ R_Z \\ C_X \\ C_Y \\ C_Z \end{Bmatrix} = \begin{bmatrix} 0 & 0 & 0 \\ 0 & 0 & 0 \\ 1 & 1 & 1 \\ 0 & 3(\frac{\sqrt{3}}{2}) & -3(\frac{\sqrt{3}}{2}) \\ -3 & 3(\frac{1}{2}) & 3(\frac{1}{2}) \\ 0 & 0 & 0 \end{bmatrix} \begin{Bmatrix} F_1 \\ F_2 \\ F_3 \end{Bmatrix}$$

2.2 Stiffness/Compliance Matrices

In the rest of the paper, the notation used will be:

R - the end effector forces in the base frame

C - the end effector moments in the base frame

ΔX - translation in the **X** direction

ΔY - translation in the **Y** direction

ΔZ - translation in the **Z** direction

$\Delta\theta_X$ - rotation about the **X** axis

$\Delta\theta_Y$ - rotation about the **Y** axis

$\Delta\theta_Z$ - rotation about the **Z** axis

In this thesis, any general motion (twist) of the platform will have six components ΔX, ΔY, ΔZ, $\Delta\theta_X$, $\Delta\theta_Y$, and $\Delta\theta_Z$. Any general force (wrench) also has six components, R_x, R_y, R_z, C_x, C_y, and C_z. We refer to these as displacements or forces along the **X**, **Y**, **Z**, $\theta_{\mathbf{X}}$, $\theta_{\mathbf{Y}}$, and $\theta_{\mathbf{Z}}$ directions respectively.

The end effector stiffness matrix describes the forces and moments that must be exerted on the upper platform to produce a given deflection of the upper platform. Because the tripod manipulator only has three degrees of freedom, one must choose which three stiffness parameters to control. By studying the workspace figures, it is obvious that the stiffnesses in the **X**, **Y**, and $\theta_{\mathbf{Z}}$ directions should not be controlled. The manipulator translates very little in the **X**, and **Y** directions and barely rotates about the **Z** axis. For these reasons, the stiffness in the **Z**, $\theta_{\mathbf{X}}$, and $\theta_{\mathbf{Y}}$ directions are controlled. The desired end effector stiffness matrix is defined below:

$$\begin{Bmatrix} R_X \\ R_Y \\ R_Z \\ C_X \\ C_Y \\ C_Z \end{Bmatrix} = \begin{bmatrix} 0 & 0 & 0 & 0 & 0 & 0 \\ 0 & 0 & 0 & 0 & 0 & 0 \\ 0 & 0 & K_Z & 0 & 0 & 0 \\ 0 & 0 & 0 & K_{\theta_Z} & 0 & 0 \\ 0 & 0 & 0 & 0 & K_{\theta_Y} & 0 \\ 0 & 0 & 0 & 0 & 0 & 0 \end{bmatrix} \begin{Bmatrix} \Delta X \\ \Delta Y \\ \Delta X \\ \Delta\theta_X \\ \Delta\theta_Y \\ \Delta\theta_Z \end{Bmatrix} \tag{2.36}$$

Note that we have chosen to decouple the forces in one direction from motions in another direction. The purpose for the end effector stiffness matrix is to define a mechanism which senses rotations and translations (twists), and produces controlled forces and moments (wrenches) to counteract the movement. In the joint space, it is much easier to sense the change in lengths, l_i, and produce controlled forces, F_i. In particular, we can implement a general control law:

$$\begin{Bmatrix} F_1 \\ F_2 \\ F_3 \end{Bmatrix} = \begin{bmatrix} k_{11} & k_{12} & k_{13} \\ k_{21} & k_{22} & k_{23} \\ k_{31} & k_{32} & k_{33} \end{bmatrix} \begin{Bmatrix} \Delta l_1 \\ \Delta l_2 \\ \Delta l_3 \end{Bmatrix} \tag{2.37}$$

where k_{ij} are joint-stiffnesses that can be arbitrarily chosen by the control system designer. The previously derived equations are recalled:

$$\begin{bmatrix} \mathbf{R} \\ \mathbf{C} \end{bmatrix} = \begin{bmatrix} \gamma_{lv}^T \\ \gamma_{l\omega}^T \end{bmatrix} \begin{bmatrix} \mathbf{F} \end{bmatrix} \tag{2.38}$$

$$\begin{bmatrix} \mathbf{i} \end{bmatrix} = \begin{bmatrix} \gamma_{lv} \mid \gamma_{l\omega} \end{bmatrix} \begin{bmatrix} \mathbf{v} \\ \omega \end{bmatrix} \tag{2.39}$$

The stiffness matrix can now be described a different way.

$$\begin{Bmatrix} R_X \\ R_Y \\ R_Z \\ C_X \\ C_Y \\ C_Z \end{Bmatrix} = \begin{bmatrix} \gamma_{lv}^T \\ \gamma_{l\omega}^T \end{bmatrix} \begin{bmatrix} k_{11} & k_{12} & k_{13} \\ k_{21} & k_{22} & k_{23} \\ k_{31} & k_{32} & k_{33} \end{bmatrix} \begin{bmatrix} \gamma_{lv} \mid \gamma_{l\omega} \end{bmatrix} \begin{Bmatrix} \Delta X \\ \Delta Y \\ \Delta Z \\ \Delta\theta_X \\ \Delta\theta_Y \\ \Delta\theta_Z \end{Bmatrix} \tag{2.40}$$

From the two derivations of the stiffness matrix, we can find the joint stiffnesses from any set of desired end effector stiffnesses, K_Z, K_{θ_X}, and K_{θ_Y}.

$$\begin{bmatrix} 0 & 0 & 0 & 0 & 0 & 0 \\ 0 & 0 & 0 & 0 & 0 & 0 \\ 0 & 0 & K_X & 0 & 0 & 0 \\ 0 & 0 & 0 & K_{\theta_X} & 0 & 0 \\ 0 & 0 & 0 & 0 & K_{\theta_Y} & 0 \\ 0 & 0 & 0 & 0 & 0 & 0 \end{bmatrix} = \begin{bmatrix} \gamma_{lv}^T \\ \gamma_{l\omega}^T \end{bmatrix} \begin{bmatrix} k_{11} & k_{12} & k_{13} \\ k_{21} & k_{22} & k_{23} \\ k_{31} & k_{32} & k_{33} \end{bmatrix} \begin{bmatrix} \gamma_{lv} \mid \gamma_{l\omega} \end{bmatrix} \tag{2.41}$$

Finding the k_{ij}'s from the desired end effector stiffness matrix poses a difficult problem. First from the given lengths, l_i, the corresponding angles would have to be calculated using

the Newton-Raphson routine. Once the angles are found, the left and right inverses of the transposed simplified Jacobian and the simplified Jacobian respectively would have to be calculated. Lastly, the k_{ij}'s would be found by multiplying the corresponding matrices. Because this process is time consuming for real time control, an alternative approach is adopted.

The joint stiffness parameters are calculated assuming the upper platform is in the home position; all link angles (θ_i) are ninety degrees. From the desired stiffness parameters, the k_{ij}'s are only calculated once. Even if the platform tilts, the k_{ij}'s are not recalculated, but still depend on the platform's home position. This method of always using one set of k_{ij}'s is appropriate if the end effector stiffness matrix does not change appreciably with changes in configuration.

A program was written which calculates the desired k_{ij}'s from the end effector stiffness parameters assuming the platform is in the original home position. It should be noted, that for any set of desired stiffness parameters, the force for one actuator depends on the change of length of all three actuators.

For the tripod mechanism, the k_{ij}'s are defined below:

$$\begin{bmatrix} a & b & b \\ b & c & d \\ b & d & c \end{bmatrix} = \begin{bmatrix} k_{11} & k_{12} & k_{13} \\ k_{21} & k_{22} & k_{23} \\ k_{31} & k_{32} & k_{33} \end{bmatrix} \tag{2.42}$$

where

$$a = 0.1111K_Z + 0.0362812K_{\theta_Y}$$

$$b = 0.1111K_Z - 0.0181406K_{\theta_Y}$$

$$c = 0.1111K_Z + 0.0272109K_{\theta_X} + 0.00907029K_{\theta_Y}$$

$$d = 0.1111K_Z - 0.0272109K_{\theta_X} + 0.00907029K_{\theta_Y}$$

The reader should remember that the forces that are being controlled are described in the fixed base frame **XYZ**. Therefore, if the upper platform tilts slightly, the force in the **Z** direction is still in the normal direction of the base frame, but its magnitude might change.

To better understand that the end effector stiffness matrix in any configuration is similar to the one based on the home position, examples are presented. For all three cases, K_Z equals 30 lbs/in, $K_{\theta_X} = K_{\theta_Y}$ equals 2 lbs in/rads. These stiffness parameters are chosen because the mechanism will now have stiffness characteristics that are desired for an ankle. An ankle is usually stiff in the approach direction and is less stiff in rotations about the axes perpendicular to the approach direction. Three cases are studied.

Case	Link 1	Link 2	Link 3
1	4 in.	4 in.	4 in.
2	4 in.	4.2 in.	3.8 in.
3	4 in.	4 in.	3 in.

In the third case, the platform is at an extreme angle, where the rotation angle $\phi = 11$ degrees, and $\alpha = -30$ degrees. In the second case, the platform still rotates, $\phi = 3.78$ degrees and $\alpha = -0.0009$ degrees. The stiffness matrices for each case are defined below. For each case, for example, the **z** axis corresponds to a different direction in the fixed base coordinate frame, because the upper coordinate frame rotates with the upper platform and the **z** axis stays normal to the surface of the upper platform. F_Z is the force in the direction of the **Z** axis and does not rotate as the platform rotates.

In the first case:

$$\begin{Bmatrix} R_X \\ R_Y \\ R_Z \\ C_X \\ C_Y \\ C_Z \end{Bmatrix} = \begin{bmatrix} 0 & 0 & 0 & 0 & 0 & 0 \\ 0 & 0 & 0 & 0 & 0 & 0 \\ 0 & 0 & 30 & 0 & 0 & 0 \\ 0 & 0 & 0 & 2 & 0 & 0 \\ 0 & 0 & 0 & 0 & 2 & 0 \\ 0 & 0 & 0 & 0 & 0 & 0 \end{bmatrix} \begin{Bmatrix} \Delta X \\ \Delta Y \\ \Delta Z \\ \Delta\theta_X \\ \Delta\theta_Y \\ \Delta\theta_Z \end{Bmatrix}$$

In the second case:

$$\begin{Bmatrix} R_X \\ R_Y \\ R_Z \\ C_X \\ C_Y \\ C_Z \end{Bmatrix} = \begin{bmatrix} 0 & 0 & 0.0287 & 0 & 0 & 0 \\ 0 & 0 & 0.0017 & -0.0011 & 0 & 0 \\ 0.0287 & 0.0017 & 30.00 & 0.0066 & -0.0002 & 0 \\ 0 & -0.0011 & 0.0066 & 1.9913 & 0.0003 & 0 \\ 0 & 0 & -0.0002 & 0.0003 & 2.0 & 0 \\ 0 & 0 & 0 & 0 & 0 & 0 \end{bmatrix} \begin{Bmatrix} \Delta X \\ \Delta Y \\ \Delta Z \\ \Delta\theta_X \\ \Delta\theta_Y \\ \Delta\theta_Z \end{Bmatrix}$$

In the third case:

$$\begin{Bmatrix} R_X \\ R_Y \\ R_Z \\ C_X \\ C_Y \\ C_Z \end{Bmatrix} = \begin{bmatrix} 0.0009 & 0.0015 & 0.1607 & -0.0041 & 0.0024 & 0 \\ 0.0015 & 0.0026 & 0.2783 & -0.0071 & 0.0041 & 0 \\ 0.1607 & 0.2783 & 29.9896 & 0.2013 & -0.1162 & 0 \\ -0.0041 & -0.0071 & 0.2013 & 1.9338 & 0.0382 & 0 \\ 0.0024 & 0.0041 & -0.1162 & 0.0382 & 1.9779 & 0 \\ 0 & 0 & 0 & 0 & 0 & 0 \end{bmatrix} \begin{Bmatrix} \Delta X \\ \Delta Y \\ \Delta Z \\ \Delta\theta_X \\ \Delta\theta_Y \\ \Delta\theta_Z \end{Bmatrix}$$

Note, the zeros in column six are actually smaller numbers of the order 10^{-5}. All three stiffness matrices have similar characteristics where the dominant values are the diagonal terms, 30, 2, and 2. Because of the physical constraints of the mechanism, ΔX, ΔY, and $\Delta\theta_Z$ cannot move independently of ΔZ, $\Delta\theta_X$, and $\Delta\theta_Y$. For example, the physical characteristics of the platform prevent a pure change in the **X** direction. A change in in the **X** direction can occur only if there is some rotation of the upper platform. The analogy is similar for ΔY, and $\Delta\theta_Z$. Because these values are so small we will assume that they are approximately equal to zero.

From the assumptions that R_X, R_Y and C_Z are small because the elements in the first, second, and third rows are small, and ΔX, ΔY, and $\Delta\theta_Z$ are very small so the elements in the first, second, and sixth column are not important, the stiffness matrix can be split into one smaller three by three matrix. For case one:

$$\begin{Bmatrix} R_Z \\ C_X \\ C_Y \end{Bmatrix} = \begin{bmatrix} 30 & 0 & 0 \\ 0 & 2 & 0 \\ 0 & 0 & 2 \end{bmatrix} \begin{Bmatrix} \Delta Z \\ \Delta\theta_X \\ \Delta\theta_Y \end{Bmatrix}$$

For case two:

$$\begin{Bmatrix} R_Z \\ C_X \\ C_Y \end{Bmatrix} = \begin{bmatrix} 30 & 0.0066 & -0.0002 \\ 0.0066 & 1.9913 & 0.0003 \\ -0.0002 & 0.0003 & 2 \end{bmatrix} \begin{Bmatrix} \Delta Z \\ \Delta\theta_X \\ \Delta\theta_Y \end{Bmatrix}$$

For case three:

$$\begin{Bmatrix} R_Z \\ C_X \\ C_Y \end{Bmatrix} = \begin{bmatrix} 29.9896 & 0.2013 & -0.1162 \\ 0.2013 & 1.9338 & 0.0382 \\ -0.1162 & 0.0382 & 1.9779 \end{bmatrix} \begin{Bmatrix} \Delta Z \\ \Delta\theta_X \\ \Delta\theta_Y \end{Bmatrix}$$

The nature of the matrices relating R_Z, C_X, and C_Y to changes in ΔZ, $\Delta\theta_X$, and $\Delta\theta_Y$ can best be understood through *stiffness ellipsoids.* The ellipsoids define the set of displacements that result in a unit force. The ellipsoid's major axes correspond to the eigenvectors of the 3 x 3 matrix. The derivation follows from the fact that the magnitude of the force equals one.

$$F^T F = 1 \tag{2.43}$$

$$F = K\delta x \tag{2.44}$$

$$x^T K^T K x = 1 \tag{2.45}$$

K is the stiffness matrix, and x is a vector corresponding to the changes of the position of ΔZ, $\Delta\theta_X$, and $\Delta\theta_Y$. The ellipsoids can be seen in Figures 2.5, 2.6, and 2.7.

The basic nature of the ellipsoid does not change much with changes in the configuration. The eigenvalues of the matrices are almost the same. Instead, it appears that the eigenvectors rotate with the platform. The motion of the eigenvectors is very hard to describe. In all cases, the eigenvector corresponding to the force in the **Z** direction remained almost exactly the same while the eigenvectors for K_{θ_X} and K_{θ_Y} seem to rotate about the **Z** axis. Interestingly, if the length of l_1 equals l_2 or the length of l_1 equals l_3, and if the corresponding other link length is changed, the eigenvectors always describe a rotation about the **Z** axis of thirty degrees. The magnitude of the change in length of the third link does not affect the eigenvectors of the small stiffness matrix. As the length is changed by

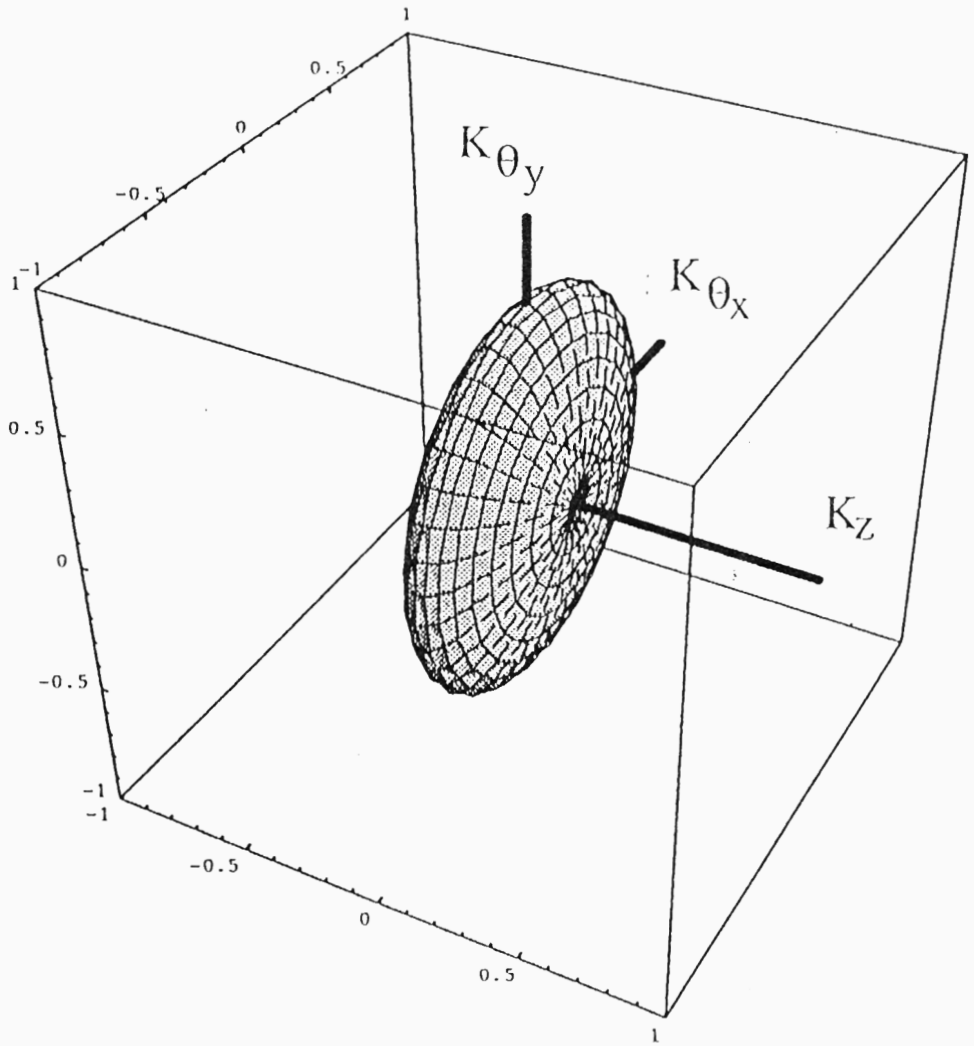

Figure 2.5: Stiffness Ellipsoid, (K_Z = 30 lbs/in, K_{θ_X} = 2 lbs in/rad, K_{θ_Y} = 2 lbs in/rad, l_1 = 4 in., l_2 = 4 in., l_3 = 4 in.)

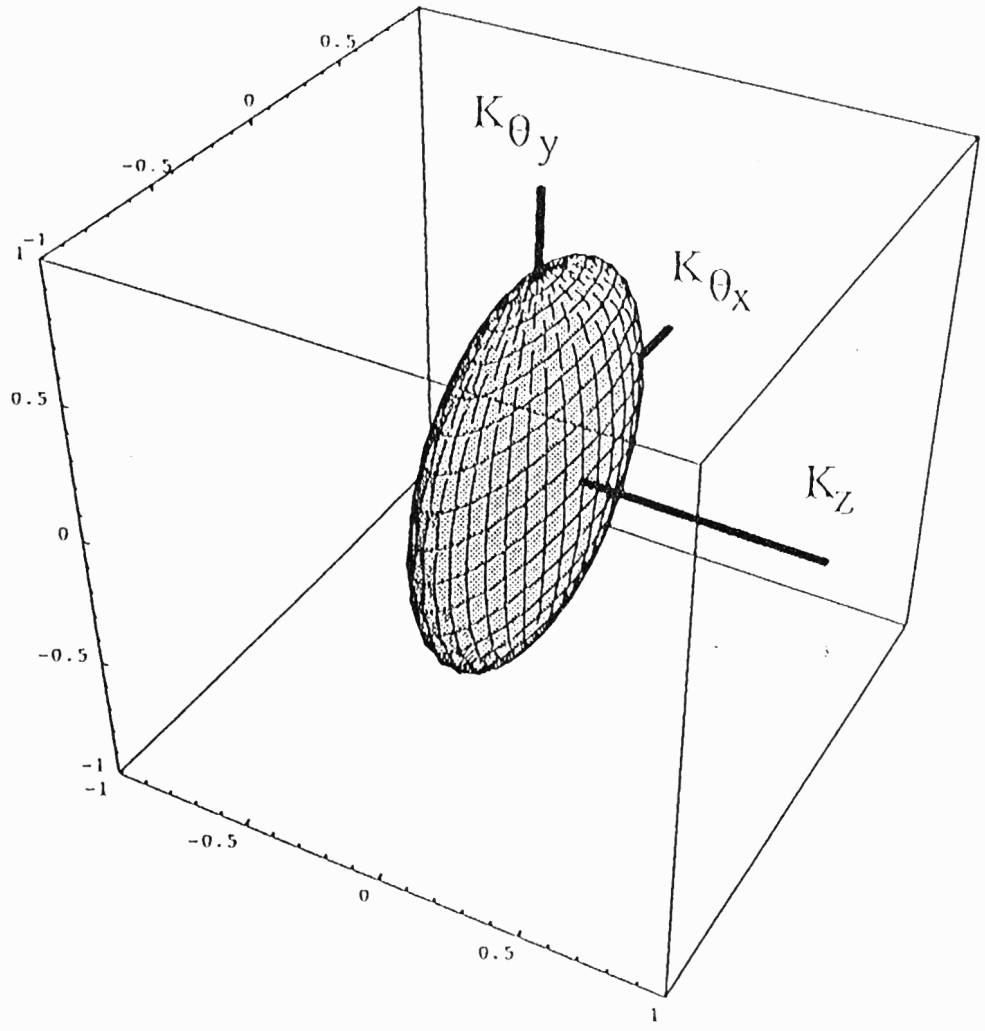

Figure 2.6: Stiffness Ellipsoid, (K_Z = 30 lbs/in, K_{θ_X} = 2 lbs in/rad, K_{θ_Y} = 2 lbs in/rad, l_1 = 4 in., l_2 = 4.2 in., l_3 = 3.8 in.)

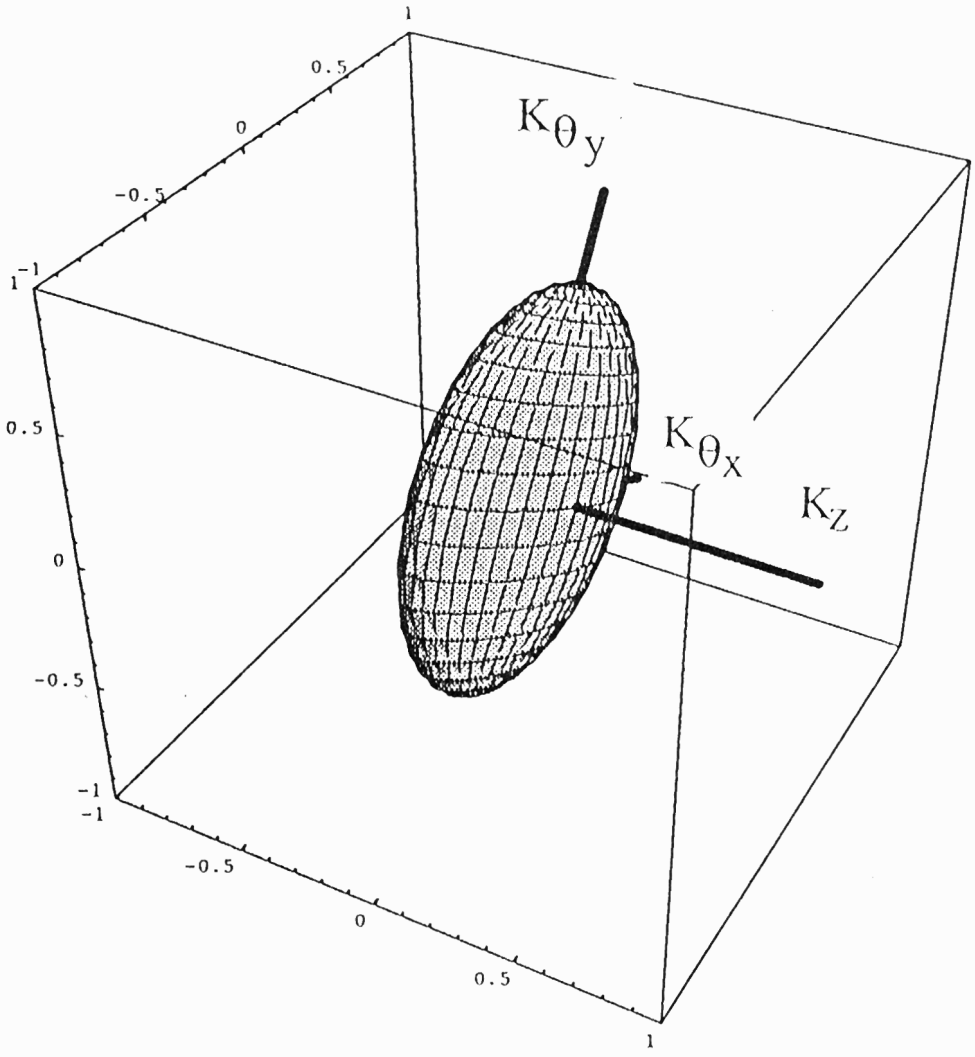

Figure 2.7: Stiffness Ellipsoid, (K_Z = 30 lbs/in, K_{θ_X} = 2 lbs in/rad, K_{θ_Y} = 2 lbs in/rad, l_1 = 4 in., l_2 = 4 in., l_3 = 3 in.)

Matrix	K_Z	K_{θ_X}	K_{θ_Y}
6 x 6	29.995	1.9099	1.99996
3 x 3	29.9915	1.9082	1.99996

Table 2.1: Eigenvalues corresponding to **Z**, θ_X, and θ_Y directions for the 6 x 6 stiffness matrix and the 3 x 3 submatrix

greater amounts, the eigenvalues do change, but very little. (Although, if l_2 equals l_3, the eigenvectors do not rotate about the **Z** axis thirty degrees.)

If this mechanism is used as an ankle, the direction of the force in the **Z** axis is very important; the force holding the leg up should remain vertical. Again, as stated before, the force corresponding to F_Z does remain vertical even if the upper platform is tilted eleven degrees. The upper platform should conform to a possibly uneven surface. Since the resulting moments in the θ_X and θ_Y directions are usually resisted by the leg, the actual rotation of these axis about the **Z** axis is unimportant.

To check the validity of using the 3 x 3 matrices, the eigensystem for the larger 6 x 6 matrices is determined for each case. The eigenvalues for the the larger matrices are very similar to the eigenvalues of the smaller matrices. For example, in the extreme case, the components of the eigenvalues are almost exactly the same as shown in Table 2.1. The components of the eigenvectors as well are almost exactly the same.

The stiffness matrices can be defined by the user, and a couple of cases for which the value of K_Z is small are presented. In the two cases K_Z equals 3 lbs/in and K_{θ_X} and K_{θ_Y} both equal 400 lbs in/rad. The behavior of the ellipsoids also changes dramatically with the change in the desired end effector stiffnesses as shown in Figures 2.8 and 2.9.

Case	Link 1	Link 2	Link 3
1	4 in.	4 in.	4 in.
2	4 in.	4 in.	3 in.

For the second case:

$$\begin{Bmatrix} R_Z \\ C_X \\ C_Y \end{Bmatrix} = \begin{bmatrix} 2.990 & 0.0534 & -0.0309 \\ 0.0534 & 386.4815 & 7.8050 \\ -0.0309 & 7.8050 & 395.4939 \end{bmatrix} \begin{Bmatrix} \Delta Z \\ \Delta\theta_X \\ \Delta\theta_Y \end{Bmatrix}$$

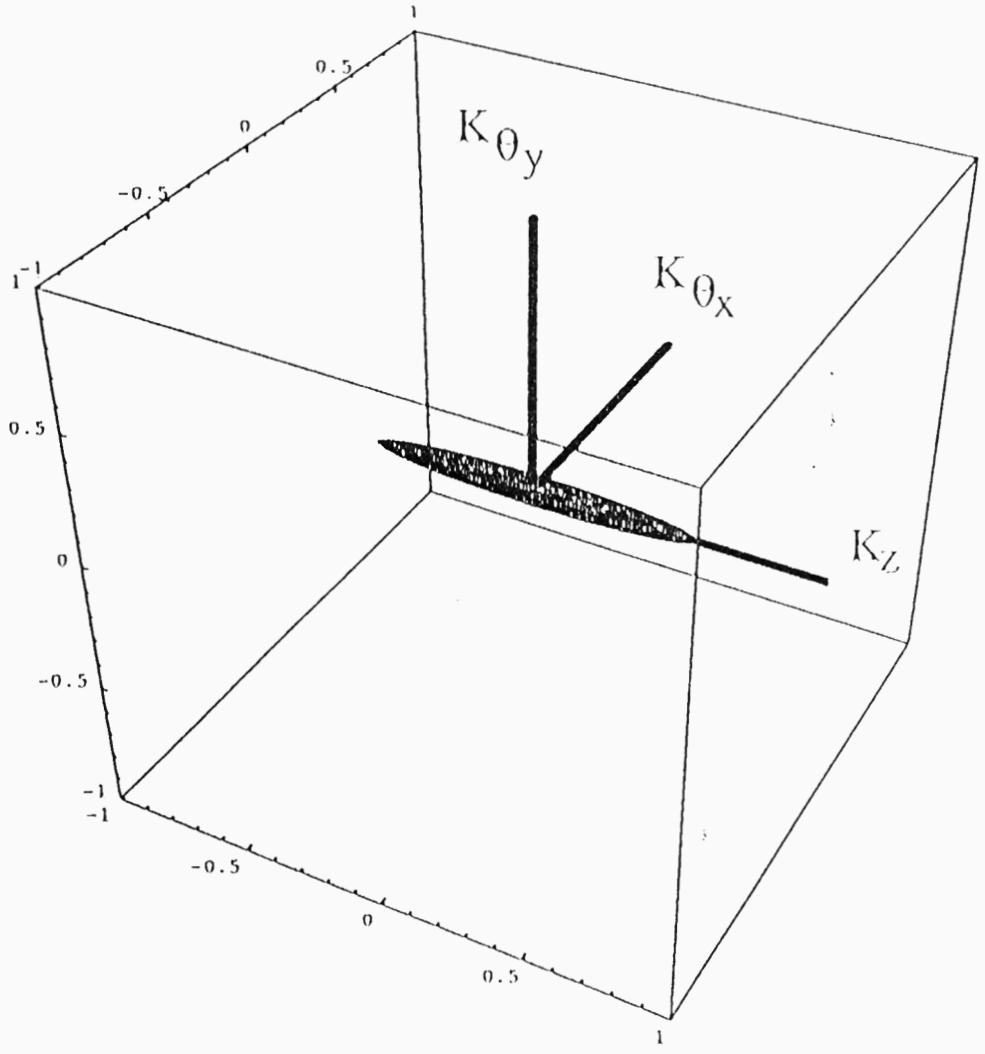

Figure 2.8: Stiffness Ellipsoid, ($K_Z = 3$ lbs/in, $K_{\theta_X} = 400$ lbs in/rad, $K_{\theta_Y} = 400$ lbs in/rad, $l_1 = 4$ in., $l_2 = 4$ in., $l_3 = 4$ in.)

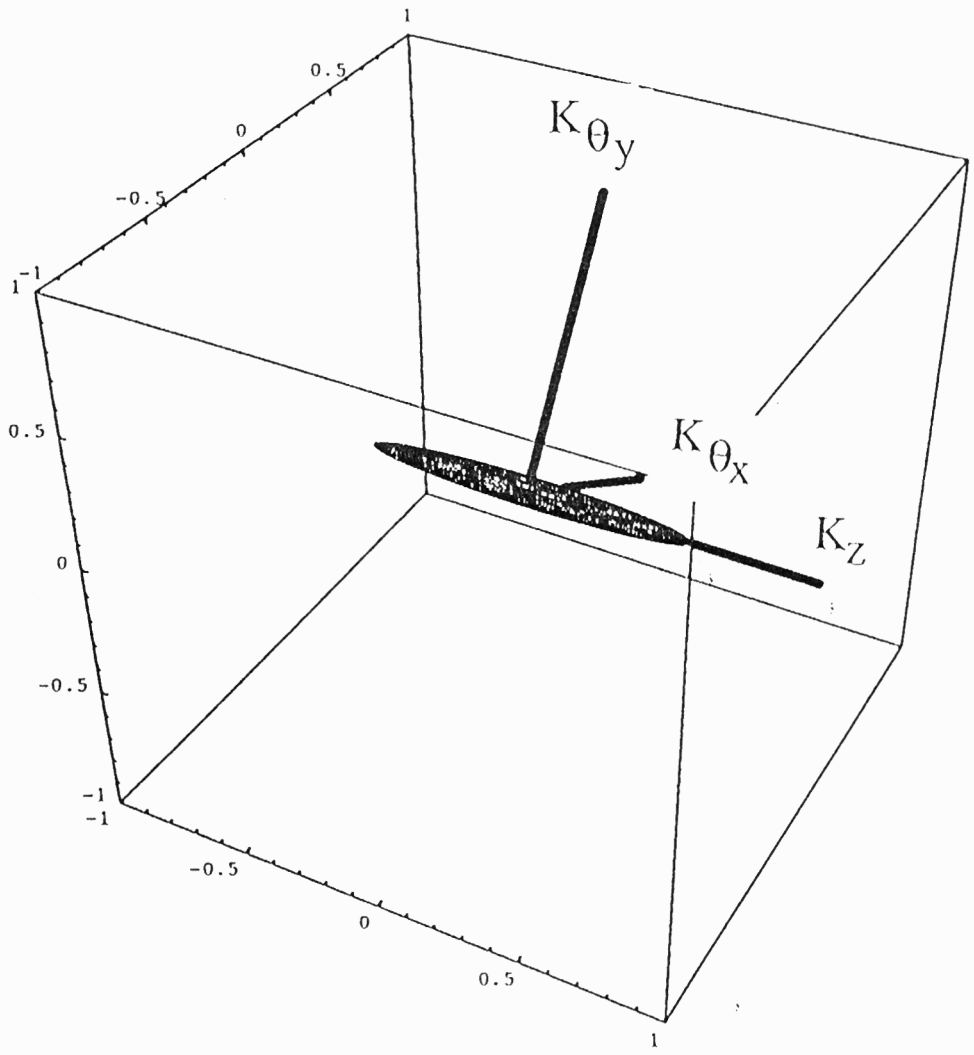

Figure 2.9: Stiffness Ellipsoid, ($K_Z = 3$ lbs/in, $K_{\theta_X} = 400$ lbs in/rad, $K_{\theta_Y} = 400$ lbs in/rad, $l_1 = 4$ in., $l_2 = 4$ in., $l_3 = 3$ in.)

Chapter 3

Important Considerations in Force Control

3.1 Theoretical and Practical Considerations in Force control

Practical and theoretical considerations for implementing force control are discussed. The main purpose of this section is to understand how to control force dynamically. With this purpose in mind, these following sections apply to controlling the force with either parallel or serial mechanisms.

Force control with serial mechanisms is researched in order to better understand how force control is currently being implemented. The traditional dynamic hybrid position/force control model relys on rigid body dynamics and relates the input forces directly to the output forces. To add dynamics to this model, integral control is used. If this algorithm for force control is chosen, then the method in which the control law is implemented using a discrete computer becomes very important. Namely, the difference rule and the gains chosen greatly affect the behavior of the overall system. Experimental and simulation results are obtained using a one degree of freedom pneumatic force controller.

Note, this work in the following section is not entirely the author's, but was done in collaboration with other researchers [20].

3.1.1 Introduction

Background

Force control is essential for the coordination of multiple actuators in an overconstrained robot system. Examples of such systems include a single robot interacting with the environment, multiple cooperating robots, and complex robot systems such as multifingered hands or walking vehicles. Although the basic idea of force control has been well-known for over a decade [22, 6], there are still some problems which are not clearly understood. Some of the limitations of force control are due to the lack of good actuators and sensors. In addition, there are several fundamental problems with the formulation and the implementation of force control algorithms. In the following sections, the theoretical and experimental results that provide an insight into these problems are discussed.

Models for Force Control

Traditionally, models for robot dynamics have been derived from principles of rigid body dynamics. As a result, the force control problem has not been formulated as a dynamic control problem. When rigid body models are employed for the robot along with ideal actuator models, the actuator inputs are related to the positions through a second order differential equation. However, the output forces are algebraically related to the actuator forces (inputs) and therefore the formulation is devoid of dynamics. In other words, there is a lack of causality in the relationship between the output forces and the inputs. At best the actuators can *compensate* for forces in a *static manner*, but they cannot *dynamically* control the forces. In fact, theories for compliance (or stiffness) control [7, 23, 28, 37], operational space control [9], hybrid control [27] and their extensions to systems with closed chains [30, 38, 41] have the same limitations. In the past these theories proved to be adequate because the focus was on performing complex tasks in a quasi-static framework as opposed to dynamic control [29, 40, 8, 15], but dynamic control is not possible with this approach.

While rigid body models are justified when robots are position controlled, interactions with dynamic environments cannot be controlled with control laws derived from such models. This difficulty with rigid body models is identified in the work in References [17, 18],

where the dynamic system is modeled by a singular system of differential equations and shown to exhibit impulsive behavior even with finite, well-behaved initial conditions. The basic idea is also recognized by Hogan and Colgate [4, 5]. They suggest that an impedance model for the contact be used for control system design.

The following sections are closely related to other work that has been done at the University of Pennsylvania. For example, force control with unilateral constraints is studied in [42] and the application to multiple arm systems is described in [12]. The extension to nonholonomic systems is presented in [44]. The work described here focuses on a more fundamental problem: the dynamic control of forces in an overconstrained system.

Organization

We study previous approaches to force control for constrained robot systems. We describe potential problems with these schemes, and point out theoretical and practical considerations that are important for the design of force control algorithms. Since most robotic controllers are implemented with a digital computer, we incorporate the effects of discretization into our analysis. The basic ideas are demonstrated with an experimental test-bed that is built with conventional (and inexpensive) actuators and sensors. We present design guidelines for force control schemes that are also applicable to stiffness control, hybrid control and simultaneous force-position control algorithms.

The paper is organized as follows: Section 3.1.2 discusses the conventional approaches to force control which relies on rigid body dynamic models. We show that an integrating compensator is absolutely essential in cases where the actuator dynamics are much faster than those of the controller. It is shown that since the integrating compensation is implemented by a digital controller, the method of discretization affects the resulting system dynamics. Section 3.1.3 develops a strategy for the opposite case where the actuator dynamics are much slower than the controller dynamics. It is clear that the actuator dynamics must be considered in the design of such controllers. Then, in Section 3.1.4, simulation and experimental data is presented to support the theoretical results of the previous sections.

3.1.2 Conventional Approaches to Force Control

Consider the force control problem of a robot system with n degrees of freedom. If I is the $n \times n$ inertia matrix, J is the Jacobian and τ is the vector of actuator forces/torques, then the dynamic equations of motion can be written as:

$$I(\theta)\ddot{\theta} + C(\theta, \dot{\theta}) + J^T F = \tau \tag{3.1}$$

where C is a nonlinear function of positions and velocities. This equation is of the form:

$$f(\theta, \dot{\theta}, \ddot{\theta}) + J^T F = \tau \tag{3.2}$$

If we decompose the input τ into τ_m and τ_f such that

$$f(\theta, \dot{\theta}, \ddot{\theta}) = \tau_m \tag{3.3}$$

$$J^T F = \tau_f \tag{3.4}$$

it is possible to design a position control scheme with τ_m as the input and a force control scheme with τ_f as the input. This is, in essence, the model used in numerous papers (see for example, [2, 3, 10, 26, 27, 30, 45]). However it is quite obvious that (3.4) is algebraic in nature and is devoid of dynamics. At best, the actuators can *compensate* for external forces in a *static* manner.

Alternatively, in the state-space formulation, Equation 3.1 is of the form:

$$\begin{aligned} \dot{x} &= A(x)\,x + B(x)\,u \\ y &= C(x)\,x + D(x)\,u \end{aligned}$$

where x, y, and u are the state, output and input, respectively. (For example, $x = [\theta^T; \dot{\theta}^T]^T$, $y = F$ and $u = \tau$.) Note that here $D(x)$ is *nonzero* unlike conventional trajectory control problems.

A Simplified Force Control Problem

In the rest of the paper, we deal with a simplified force control problem in one dimension. Consider the equation:

$$y(t) = D\,u(t) \tag{3.5}$$

where D is a constant relating input force/torque u to output force y. Throughout this paper it is assumed that $D > 0$. This equation, like Equation 3.4, does not include any actuator dynamics and employs a rigid body contact model.

The dynamics of the actuator and the dynamics of contact interaction can also be explicitly modeled. For example, if these can be adequately represented by a second order system (natural frequency ω_a, damping ratio ζ_a and steady-state gain D), the output force is related to the input by the equation:

$$\frac{1}{\omega_a^2}\frac{d^2y}{dt^2} + \frac{2\zeta_a}{\omega_a}\frac{dy}{dt} + y = Du \tag{3.6}$$

or using Laplace transforms:

$$\frac{Y(s)}{U(s)} = \frac{D}{\frac{s^2}{\omega_a^2} + \frac{2\zeta_a s}{\omega_a} + 1} \tag{3.7}$$

The simplified model in Equation 3.5 is a valid approximation to the system in Equation 3.6 provided ω_a is very large. If the desired force y_d is given, the input u can be calculated as:

$$u(t) = \frac{y_d(t)}{\tilde{D}} \tag{3.8}$$

where $\tilde{D}$ is the estimated (modeled) value of D. The relation of the output to the desired output is given as:

$$y(t) = \frac{D}{\tilde{D}}\, y_d(t) \tag{3.9}$$

Clearly, if $\tilde{D} = D$, nothing further needs to be done. But, if there is a discrepancy, then there is always a finite error. (This discrepancy could be attributed to calibration errors, inaccuracies in modeling, parameter drift, noise, etc.) Thus there is a need for a feedback control scheme and this is the subject of the next several subsections.

Proportional Control

The simplest feedback law is obtained as follows:

$$u(t) = \frac{y_d(t)}{\tilde{D}} + K_p(y_d(t) - y(t)) \tag{3.10}$$

where K_p is the proportional control gain. Substitution into Equation 3.9 yields

$$y(t) = \frac{DK_p + \frac{D}{\tilde{D}}}{DK_p + 1} y_d(t) \tag{3.11}$$

If there is no noise, for large K_p, the error is close to zero and it is easy to conclude that forces can be controlled by proportional control.

This analysis is not quite complete because the control law given by Equation 3.10 with the model of Equation 3.9 leads to a system which is static and therefore characterized by algebraic equations. It is meaningless to talk about the stability or convergence of such schemes. The potential practical problems with this scheme are evident when we try to implement such a scheme with computer control. (The effects of discretization are discussed in Section 3.1.2 and it is shown that the proportional gain is limited to $\frac{1}{D}$ for stability.)

Proportional plus Integral Control

In the above analysis, since the only possible problem with proportional control is the presence of a steady-state error (there is no transient in a static system), it is natural to add the integral of the error in the feedback loop. This has been the basic approach in [3, 10, 45], although these papers did not clearly justify the need for the integral component.

This elimination of steady state error is one advantage. The second advantage of employing integral control is that it does introduce causality into the system [35]. The control law

$$u(t) = \frac{y_d(t)}{\tilde{D}} + K_I \int (y_d(t) - y(t))\, dt + K_p(y_d(t) - y(t)) \tag{3.12}$$

leads to the following input-output equation in s-domain:

$$Y(s) = Y_d(s) \left(\frac{s\left(\frac{1 + K_p\tilde{D}}{K_I\tilde{D}}\right) + 1}{s\left(\frac{1 + K_pD}{K_I\tilde{D}}\right) + 1} \right) \tag{3.13}$$

The need for using dynamic state feedback for force control has been formally justified in an earlier paper [43, 12], and the use of such a scheme has been demonstrated for multiarm control in [42, 12, 21]. In fact, it is shown in these papers that a pure integral control scheme ($K_p = 0$, $K_I \neq 0$) ensures stability, and simulations are presented to illustrate the robustness of the approach.

Discrete Control Laws

While continuous system theory explains the effect of proportional and integral gains, it is beneficial to investigate the effects of discretization which are inevitable in digital controllers. We assume a digital control system in which the sampling interval is T_s and the sampling frequency is ω_s. Of course, a rigid body model is justified only if the frequencies of operation are much smaller than the natural (characteristic) frequency of the physical system ω_a. Since the frequency of operation is limited by the Nyquist frequency, it is safe to state that a rigid body approximation can be employed whenever $\omega_s \ll \omega_a$. In fact, the exact requirement is that the delay τ_d between the controller's output (commanded voltage) and input (measured error signal) must be greater than the settling time of the actuator due to a step input. In what follows we consider the effects of discretization on static and dynamic feedback schemes.

In the case of integral control, since the controller introduces causality into an otherwise static system, the method of discretization is particularly important. For example, consider the systems obtained by using two candidate difference rules — the backward difference rule and the trapezoidal difference rule:

$$s = \frac{z\ -\ 1}{Tz}; \quad s = \frac{2}{T}\left(\frac{z\ -\ 1}{z\ +\ 1}\right) \tag{3.14}$$

where z^{-1} is the discrete delay operator and T is the controller sampling period.

The discrete control law must be causal, which restricts the calculation of u to be a function of the physical system data from the *previous* sample periods. However, this restriction does not apply to the desired variable y_d because it may be known *a priori.* Thus, the discrete control law is a function of the form:

$$u(k)\ =\ \mathcal{F}(\ y(k-i),\ y_d(k),\ y_d(k \pm i)\ ) \qquad i \geq 1 \tag{3.15}$$

The substitution of the backward and trapezoidal difference rules into Equation 3.12 while satisfying Equation 3.15 yields the discrete control laws:

$$u_{back}(z) \ = \ \frac{y_d(z)}{\tilde{D}} \ + \ K_I\left(\frac{T}{z\ -\ 1}\right)(y_d(z) - y(z)) \ + \ K_p\left(z^{-1}\right)(y_d(z) - y(z)) \tag{3.16}$$

$$u_{trap}(z) \ = \ \frac{y_d(z)}{\tilde{D}} + K_I\frac{T}{2}\left(\frac{z+1}{z-1}\right)\left(z^{-1}\right)(y_d(z) - y(z)) + K_p\left(z^{-1}\right)(y_d(z) - y(z)) \tag{3.17}$$

where Equations 3.16 and 3.17 correspond to the use of the backward and trapezoidal difference rules, respectively.

These control laws are then applied to the discrete form of the continuous system model (Equation 3.5) given as:

$$y(z) = D\,u(z) \tag{3.18}$$

which results in the discrete transfer functions:

$$y(z) = y_d(z)\left(\frac{D}{\tilde{D}}\right)\left(\frac{z^2 + (K_I T\,\tilde{D} + K_p\tilde{D} - 1)z - K_p\tilde{D}}{z^2 + (K_I T\,D + K_p D - 1)z - K_p D}\right) \tag{3.19}$$

$$y(z) = y_d(z)\left(\frac{D}{\tilde{D}}\right)\left(\frac{z^2 + (\frac{K_I T\tilde{D}}{2} + K_p\tilde{D} - 1)z + \frac{K_I T\tilde{D}}{2} - K_p\tilde{D}}{z^2 + (\frac{K_I T\,D}{2} + K_p D - 1)z + \frac{K_I T\,D}{2} - K_p D}\right) \tag{3.20}$$

where Equation 3.19 is derived with the backward rule and Equation 3.20 uses the trapezoidal rule.

The above systems are stable when the poles of the Equations 3.19 and 3.20 are within the unit circle of the Z-plane. This stability condition bounds the values of K_I and K_p, and the boundaries vary significantly depending on the difference rule employed. For the backward difference rule, the stability bounds are

$$\|K_p D\| < 1\,, \quad \|\frac{K_I T\,D}{2} + K_p D\| < 1\,, \quad K_I > 0 \tag{3.21}$$

and the bounds for the trapezoidal difference rule are

$$\|K_p D\| < 1\,, \quad \|\frac{K_I T\,D}{2} - K_p D\| < 1\,, \quad K_I > 0 \tag{3.22}$$

These boundaries and the "stable" regions are depicted on the plane of $K_p D$ versus $K_I T\,D$ in Figure 3.1. Note these bounds can be found using Jury's rule.

The range of allowable gains shown in Figure 3.1 can be subdivided into four regions. These different regions correspond to different locations of the poles within the unit circle. Region I contains the underdamped poles, and Region II contains the overdamped poles. The remaining regions have one (Region III) or both (Region IV) poles on the negative real axis of the Z-plane. A pole located on this part of the Z-plane corresponds to a pole in the

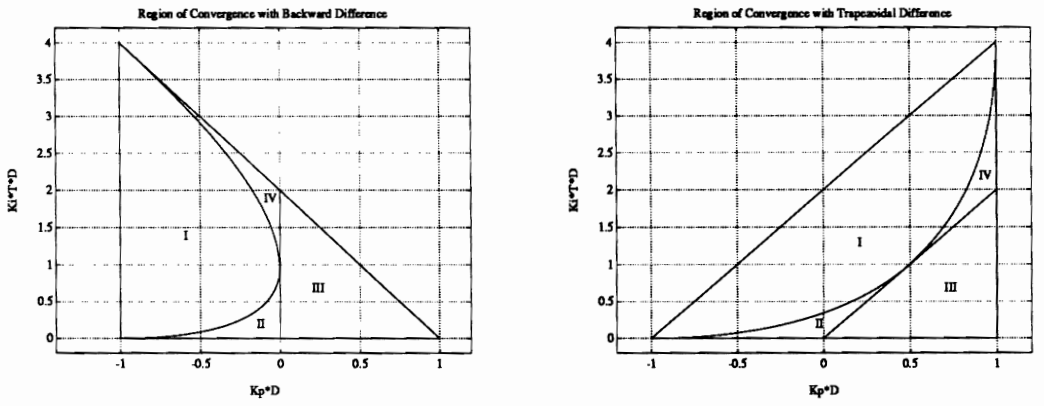

(a) (b)

Figure 3.1: Region of Convergence for (a) Backward and (b) Trapezoidal Difference Systems

s-plane of the form $s = a \pm i\omega_s/2$ where $-\infty < a \leq 0$ and ω_s is the sampling frequency. The point where all four internal regions intersect corresponds to two poles at $z = 0$ in the Z-plane.

From the figures we can make the following observations. First, the gain for a proportional control scheme (the $K_I = 0$ axis) is severely limited. A stable response requires $\|K_p D\| < 1$. Secondly, the possibly counterintuitive conclusion can be made that a negative K_p is admissible [1]. In fact, a standard first order exponentially decaying response requires a negative K_p (resulting in a single pole on the positive real axis of the Z-plane). Finally, with the addition of an integral component the system can exhibit a wide range of second order responses. This is true, even if K_p is zero resulting in a pure integral control law.

Figure 3.2 is a magnified view of Regions I and II for the trapezoidal case and provides a guideline in designing the response of system. The values of K_I and K_p can be estimated from Figure 3.2.a for a desired underdamped system response characterized by a damping ratio L (ζ) and a natural frequency Wn (ω_n). Figure 3.2.b can be used to estimate K_I and K_p for an overdamped system response characterized by the time constants Tau1 and Tau2

[1] If a more complete model that includes the position trajectory is examined, a negative proportional gain affects a stable position control subsystem by increasing the inertia of the system, but the subsystem remains stable.

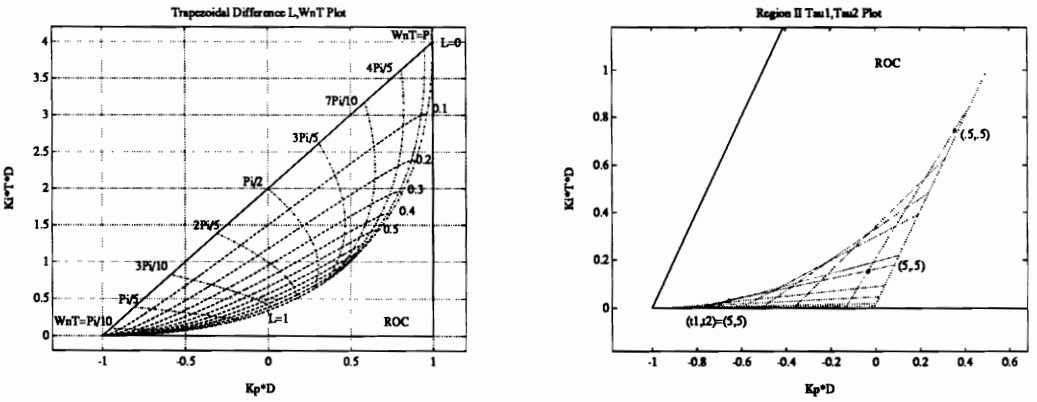

(a) (b)

Figure 3.2: Choosing Gains from System Specifications for Trapezoid Difference Implementation

(τ_1 and τ_2). It is important to note that each axis in Figure 3.2 is scaled with respect to the system variable D. Since it is assumed that this value is not exactly known, it's estimate $\tilde{D}$ can be used for selecting gains for control system design. But it should be remembered that the resulting values for K_I and K_p will correspondingly only be *estimates* of gains for the desired response parameters.

The plots in Figure 3.3 show the step response for the Trapezoidal difference rule implementation. A representative graph of each region is shown for two different $\tilde{D}/D$ ratios (.7 and 1.3). In each case, since $K_I \neq 0$, the system exhibits a steady state error of zero for a unit step input.

3.1.3 Force Control with a Causal Model

When the assumption $\omega_s \ll \omega_a$ is not valid, there is no justification for using the acausal model in Equation 3.1. It is essential to incorporate a model of the actuator dynamics, such as the one in Equation 3.7, into the control system design. It is clear that the input is now causally related to the output. We examine the implications and the effect of errors caused by approximate models using the example of a single degree-of-freedom pneumatic force controller. We later substantiate the theoretical analysis with simulations and experimental data.

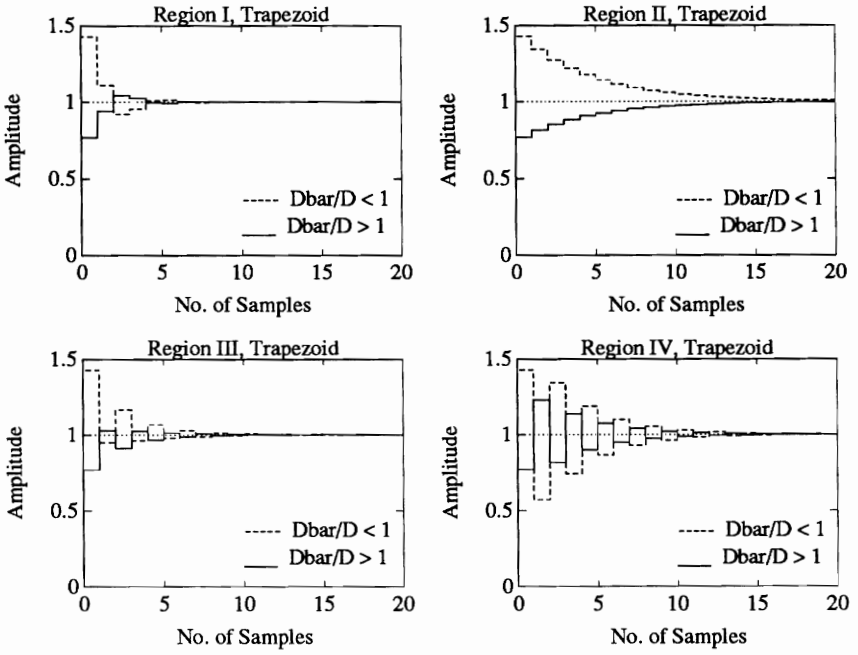

Figure 3.3: Input step response with Trapezoidal Difference Rule.

Example of a pneumatic force controller

We consider a double-ended, linear, pneumatic actuator with a force sensor. The actuator consists of two single-ended, graphite-glass cylinders (without seals). The actuator is driven by a flow-control valve and the differential pressure in the cylinders is fed back through an analog proportional loop in order to enhance the force controllability. The force control law is implemented on a PC-AT compatible computer. The block diagram for the control scheme is presented in Figure 3.4. A detailed description of the experimental test-bed is presented in the section 3.1.5.

Analytical modeling of pneumatic systems is quite difficult. The primary reasons are the compressibility of air, variation of the system parameters with temperature which increases with time, and nonlinearities due to friction at the seals [24, 31]. (The experimental test-bed uses graphite-glass cylinders which does minimize the effects of friction.) Instead, we adopt an experimental approach in which we use standard system identification techniques to develop an experimental model.

The open-loop model for the valve, actuator, inertia, force sensor and the contact is

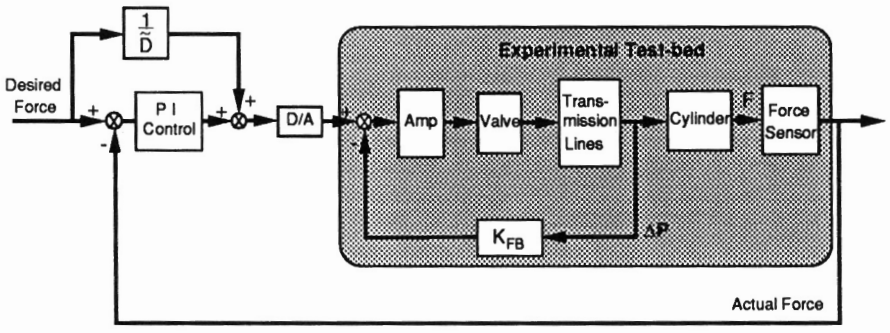

Figure 3.4: Block diagram of pneumatic control system

developed through random noise testing. The input to the valve is random noise while the output is the voltage recorded at the force sensor. A Hewlett-Packard dynamic signal analyzer facilitated this process. An integer math routine is written which converts the six strain gage readings into the actual applied force. The sampling frequency of the system is 550 Hz. Thus the models obtained are accurate to a frequency of approximately 55 Hz. The models represent our system well because the natural cuttoff frequency is less than 16 Hz, see section 3.2. The open-loop model does have an inner feedback loop that is accomplished by the analog feedback of the cylinder pressure as shown in Figure 3.4. The inner feedback gain K_{fb} can be varied between zero and one. The frequency response obtained for this system is shown in Figure 3.5 for two different (analog) feedback gains. (Broadly speaking, the larger the feedback gain, the better the performance of the closed loop force controller). In each case, models for the system were obtained through curve fitting. These transfer functions are:

1. $K_{fb} = 0.5$

$$\frac{Y}{U}(s) = \frac{14185(s + 90.7)\exp^{-0.02s}}{(s + 9.2)(s + 26)(s^2 + 36.3s + 6338)} \tag{3.23}$$

2. $K_{fb} = 1.0$

$$\frac{Y}{U}(s) = \frac{26855(s + 86.6)\exp^{-0.02s}}{(s + 19.3)(s + 25)(s^2 + 26.5s + 6031)} \tag{3.24}$$

Note that these transfer functions are obtained with small signal testing so that the linear model assumption is valid. Approximate analytical models and experimental validation are

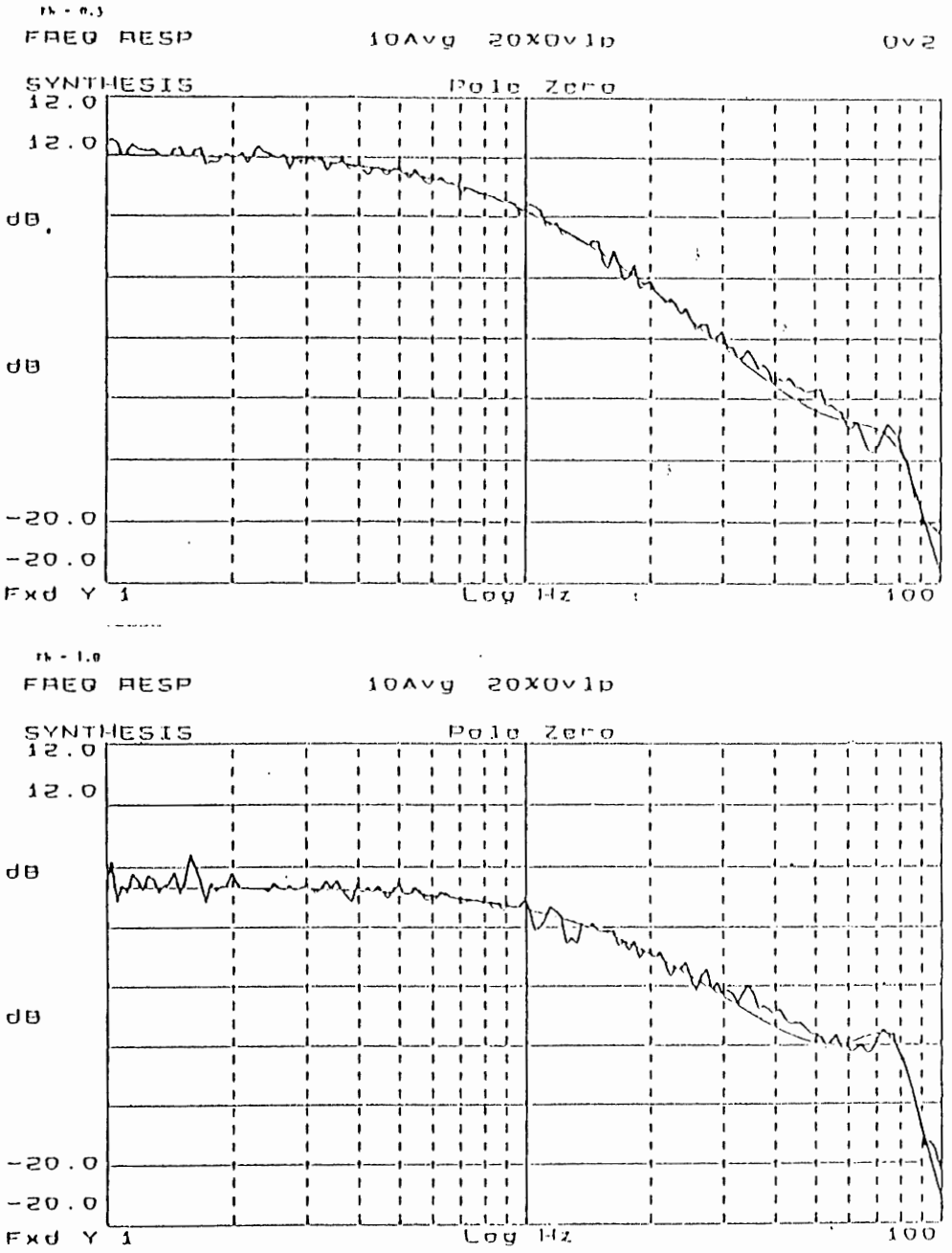

Figure 3.5: Frequency response of the pneumatic system for K_{fb} equal to 0.5 and 1.0.

discussed in [31]. We also note that while a higher order systems may produce an arguably better match when fitted to the actual system data, such a procedure does not completely eliminate modeling errors. Further, higher order fits also result in a more complex model which complicates controller design and simulation.

The transfer function does describe a nonminimum phase system. Nonminimum phase systems are slow in response because of the excessive phase lag. Our system's nonminimum phase behavior is attributed to a transport lag which occur in pneumatic systems [19].

Control laws

Pursuing the example of the pneumatic force controller further, we can see both models of Equation 3.23 and 3.24 result in causal (non-algebraic) relation between the input and the output. A variety of feedback control algorithms can be designed for such a system. We prefer the simple proportional and proportional plus integral control laws for the following reasons. First, an accurate experimental model is not likely to be available. Sophisticated model-based controllers such as those based on inverse dynamics schemes are not necessarily superior when the model is not completely correct. Second, the main objective of this section is to investigate the possible perils with rigid-body, acausal assumptions and the simple control laws that are used with such models. Finally, even with sophisticated models, in many cases, such simple controllers prove to be satisfactory.

3.1.4 Experiments with Force Control

In this section, we examine the performance of different control laws. We present simulation results obtained with the analytical models in Equations 3.23 and 3.24 and experimental results obtained from the test-bed. The trapezoidal difference rule is implemented in the digital control law of both the experimental test-bed and the simulation. Two cases are investigated:

1. Case 1: The sampling frequency is well below the characteristic frequency of the system ($\omega_s \ll \omega_a$)

2. Case 2: The system dynamics are much slower than the sampling frequency ($\omega_a \ll \omega_s$)

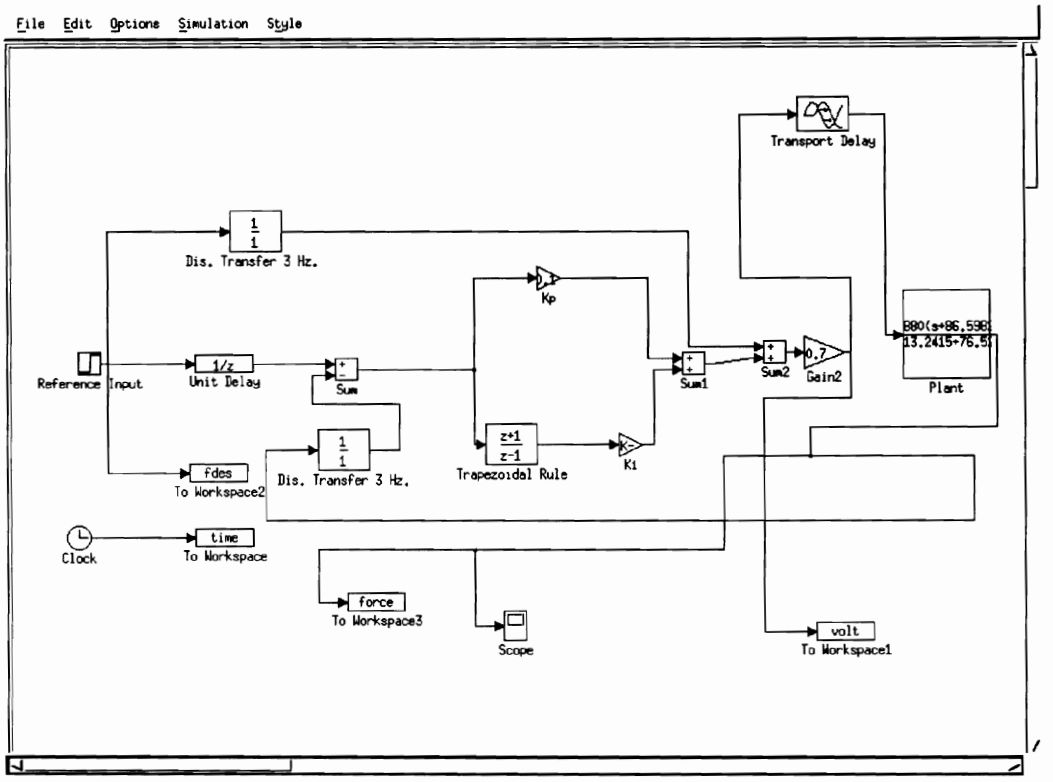

Figure 3.6: Block Diagram of Simulation

In each case, the results are compared and discussed with relation to the analysis in the previous sections. The simulation is implemented with the MATLAB software package.

Simulation

A computer simulation was developed using SIMULAB which allows the user to choose discrete blocks as well as continuous blocks. The controller is implemented using discrete blocks while the system is implemented as a continuous transfer function. The actual simulation is shown in Figure 3.6.

The experimental transfer function referred to as the plant is implemented using a continuous block. The reference input to the system is a step input. The unit delay block is used to delay the error one discrete sample period. The trapezoidal block describes the discrete integrator that was used. The other discrete transfer function blocks were used to simulate the actual digital input output board.

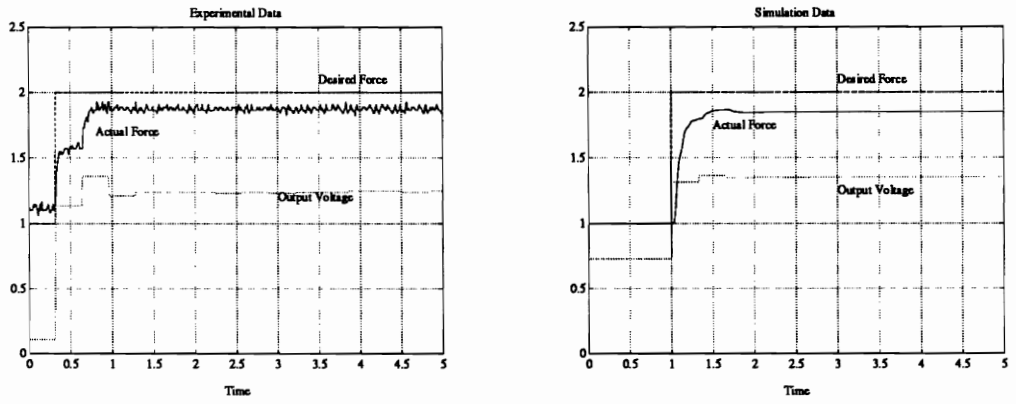

(a) (b)

Figure 3.7: Case 1: Proportional control with $K_I T \tilde{D} = 0$, $K_p \tilde{D} = 0.4$.

Three important points can be seen from the simulation model. First the desired force is fed forward with no delay. This is possible because the desired value is known ahead of time. Secondly, the error is delayed one sample period. The control signal is updated immediately at the start of the sample period, but the value sent is calculated one sample period before. After the control signal is updated, the control signal which will be sent out at the start of the next sample period is calculated. By using this method, it is assured that the control signal is updated exactly one sample period apart. Finally, the actual output is not delayed a sample period. In the computer, the system is actually sampled at 150 Hz, but the control law is only implemented every 3 Hz for the $\omega_s \ll \omega_a$ case. The actual output value that is used for the next control law is the value at the end of the previous 3 Hz sample period. By this time, the system response is completely steady.

Case 1

In this case, the physical system reacts much quicker than the digital controller. Here it is meaningful to apply the analysis of Section 3.1.2 where the input torque and output force are algebraically related. This case is realized by restricting the digital controller to a sampling rate of 3 Hz, well below the bandwidth of the actuator system with $K_{fb} = 1$ (approximately 16 Hz.).

In the following figures, the simulation and experimental data are organized side by side

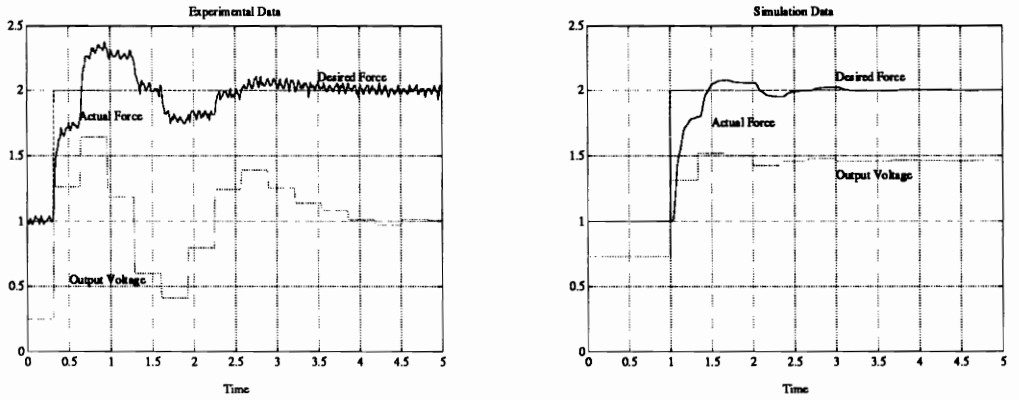

(a) (b)

Figure 3.8: Case 1: Underdamped response with $K_I T\,\tilde{D} = 2.2$, $K_p \tilde{D} = 0.6$.

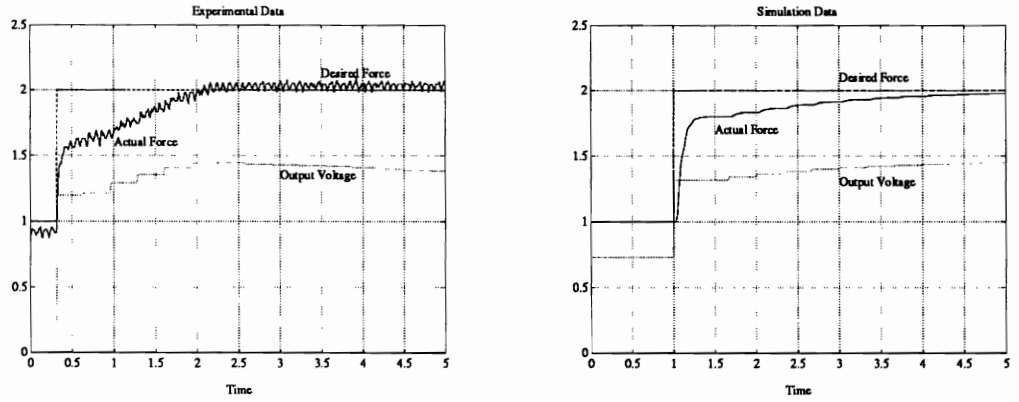

(a) (b)

Figure 3.9: Case 1: Overdamped response with $K_I T\,\tilde{D} = 0.2$, $K_p \tilde{D} = -0.1$.

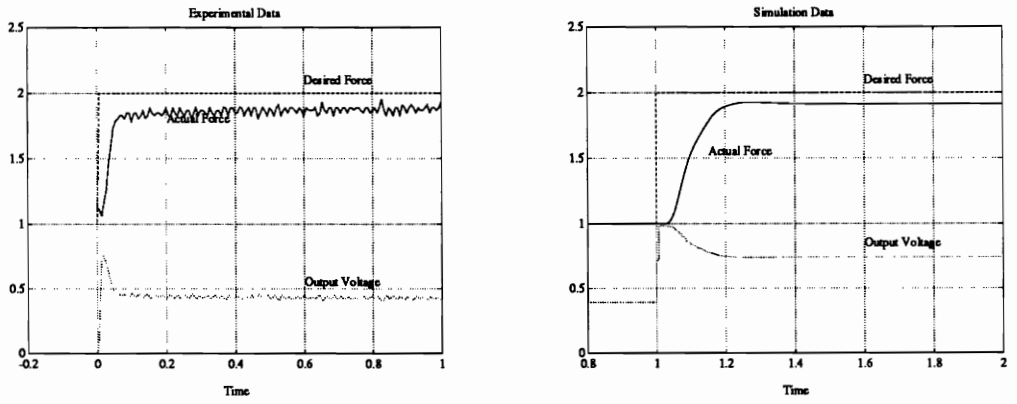

(a) (b)

Figure 3.10: Case 2: Proportional control with $K_I = 0$, $K_p = 0.8$.

for the same tests. The simulation is based on the actuator model derived from experiments as shown in Equation 3.24. Each plot depicts the actual force (in lbs.) measured by the sensor as a solid line, the desired force signal (in lbs.) as a dashed line, and the output signal of the digital controller (in volts) as a dotted line.

Figure 3.7 shows the step response with $K_I = 0$ and $K_p\tilde{D} = 0.4$. Note in this case that the experimental data and the simulation both show (as predicted by the theory) a steady state error due to $\frac{\tilde{D}}{D} \neq 1$. When K_I is used, the steady state error is eliminated, as expected. Figures 3.8 and 3.9 show the step response for Regions I and II. The underdamped response (Region I) is obtained with $K_I T\,\tilde{D} = 2.2$ and $K_p\tilde{D} = .6$ while the overdamped response (Region II) has gains $K_I T\,\tilde{D} = 0.2$ and $K_p\tilde{D} = -0.1$. A comparison of these plots with Figure 3.3 shows that they are also in accordance with the theoretical analysis of Section 3.1.2.

Case 2

This section presents the case in which the sampling frequency of the digital controller is much larger than the bandwidth of the physical system. To realize this large difference between the sampling frequency and the actuator's bandwidth, the analog feedback of the physical system (K_{fb}) is set to 0.5 and the digital controller of the both the experimental test-bed and the simulator samples at 150 Hz. The simulation incorporates the actuator

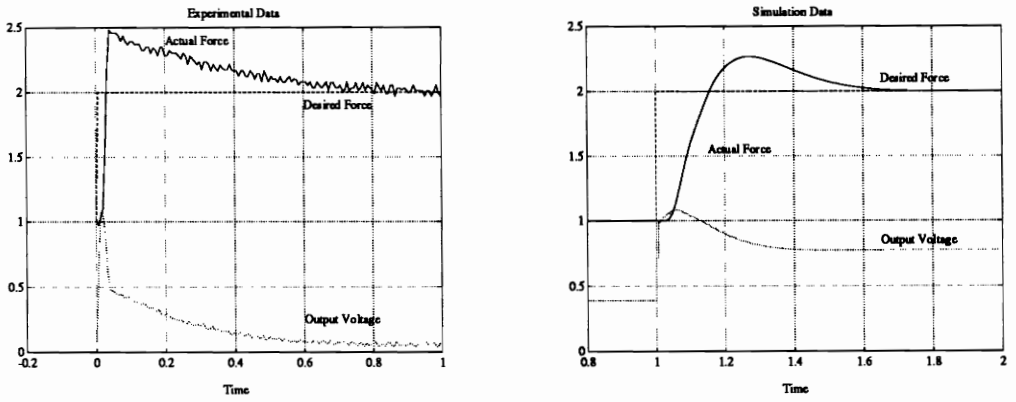

(a) (b)

Figure 3.11: Case 2: Integral and Proportional control with $K_I = 8.0$, $K_p = 0.8$.

model that is derived from the measured frequency response (Equation 3.23).

Again, simulation and experimental data for the same tests are presented in each figure and the solid line is the actual force, the dashed line is the desired force, and the dotted line is the digital controller output. The first plot (Figure 3.10) shows the response of the system with only proportional compensation. There is a non-zero steady state error. As K_p is increased, the physical system becomes unstable.

Figure 3.11 depicts a trial with integral and proportional compensation ($K_p = 0.8$ and $K_I = 8$). The results show a response in which the error converges toward zero. The type of behavior exhibited in these plots does not reflect the analysis of Section 3.1.2 because the basis of that analysis is an instantaneous model and in this case the physical system certainly has a causal response.

The discrepancies between the experimental and simulated data reflect the difficulties in finding simple and accurate models for the pneumatic system. In particular, the modeling errors in the high frequency range (above 50 Hz.) are significant. The main sources of error are thought to be the friction in the servovalve and the actuator cylinder, the compressibility of air and the change in the thermodynamic properties caused by the increase in temperature over time.

Summary

We have shown through computer simulation and experimentation that

- The approach to force control with an acausal model is fraught with perils. At the very least it is necessary to include an integrator in the control law. Further, the effect of discretization must be thoroughly investigated. The dynamics of the system is a strong function of the implementation of the control law.
- The design of control laws (and the selection of gains) based on a rigid body model and an algebraic actuator model (as presented in Section 3.1.2) is only valid when $\omega_s \ll \omega_a$.
- In the case when $\omega_a \ll \omega_s$, the model is causal. Here force control schemes can be designed using the conventional approach. Obtaining actuator models can be difficult. However, with a knowledge of a characteristic frequency for the system, it is possible to select gains so that simple control laws yield the desired performance.

Although the system studied is pneumatically actuated, the same basic principles apply to electrical and hydraulic actuators as well. In most conventional robot arms, DC servo motors are used as actuators. Typically they have a higher control bandwidth (under low loads) and with rigid effectors and environment, ω_a is very high. Thus most typical situations fall into the Case 1 category and the theoretical analysis in Section 3.1.2 is directly applicable.

3.1.5 Description of the Experimental System

The single degree of freedom pneumatic system consists of three major components, the valve / actuator mechanism, the computer and the amplifier.

The valve / actuator system is designed with off-shelf-components. Graphite glass actuators (Airpot) are used in order to minimize friction. Since only single-acting graphite-glass actuators are commercially available, and double acting action is desired, two actuators acting in opposite directions are used.

A flow control valve, Atchley 204, is used to control the flow of air. This valve adjusts the flow of air for a given voltage (If a zero voltage is commanded, the flow of air is stopped).

The spool type valve consists of a flapper whose position is adjusted by a torque motor. The torque motor is controlled by an amplifier, which converts a signal of plus or minus ten volts to plus or minus ten milliamperes of current. The amplifier board also has an analog feedback loop which is needed for pressure feedback. Without pressure feedback, the static force-voltage calibration curve is very steep thus making force control virtually impossible. Pressure feedback is accomplished by two pressure transducers, SenSym 1620A, which are mounted at the inlet to the actuators. With the feedback, the force-voltage curve is flatter and quite linear. The valve to actuator distance is minimized by mounting the valve close to the actuators. This reduces the intermediate volume of air which in turn minimizes delays in the transmission line. and improves the performance of the system.

The force feedback is accomplished by a force sensor purchased from Zebra Robotics, Inc. The force sensor has six strain gauges and outputs six digital signals. The strain gauge readings are decoupled using a calibration matrix.

Data acquisition is done with an AT-computer using a data acquisition board and a digital input/output board. The digital I/O board is used to input the six strain gauge signals. The data acquisition board is used to output a voltage signal to the amplifier which controls the valve. The control program is written in C.

3.2 Improvements with Pneumatic Force Control

As stated in Section 1.2.2, both Bobrow and Mannetje include an inner pressure feedback loop in order to improve the overall performance of the pneumatic position control system. In order to improve the force control, inner pressure feedback is added to the one degree of freedom testbed, see Figure 3.4. An experimental approach to modeling the system which includes the flow control valve, pressure transducers, and the surface contact is adopted. A description of how the system is modeled experimentally by using a signal analyzer is given in Section 3.1.3.

The inner feedback gain is varied and the system model is obtained experimentally to determine whether the feedback increases the natural cutoff frequency of the force control system. It is easily shown that when the feedback is applied to a simple first order system, the overall gain of the system decreases but the performance of the system increases. The

Feedback Gain	Magnitude at 1 Hz. (dB)	Natural Cutoff Frequency (Hz)
0.0	24	1.7
0.5	8	8.7.
1.0	4	16.3

Table 3.1: Experimental Results using Inner Feedback for Force Control

performance increases because the time constant decreases; the dynamics of the system are changed. Experimental Bode plots of our system with the inner feedback gain set to 0, 0.5, and 1 are presented in Figure 3.12. The natural cutoff frequency of the system is determined by choosing the frequency corresponding to a three dB drop off from the original magnitude. Table 3.1 presents the experimental findings.

The magnitude of the system drops approximately six times, but more importantly, the natural cutoff frequency is increased by approximately nine times. The bandwidth of the system can be varied from 2 Hz. to 16 Hz by changing the inner feedback gain.

By increasing the gain, the input voltage to output force relationship changes. The curve becomes flatter and more linear. Because the curve becomes flatter, the input to the system can be increased without saturating the system. For example, two volts might correspond to the maximum output of twenty pounds. A system with a larger feedback gain, might require an input of ten volts to obtain the same maximum output. By increasing the input to the system, the larger output force can still be obtained. This methodology only applies until the maximum input voltage is exceeded.

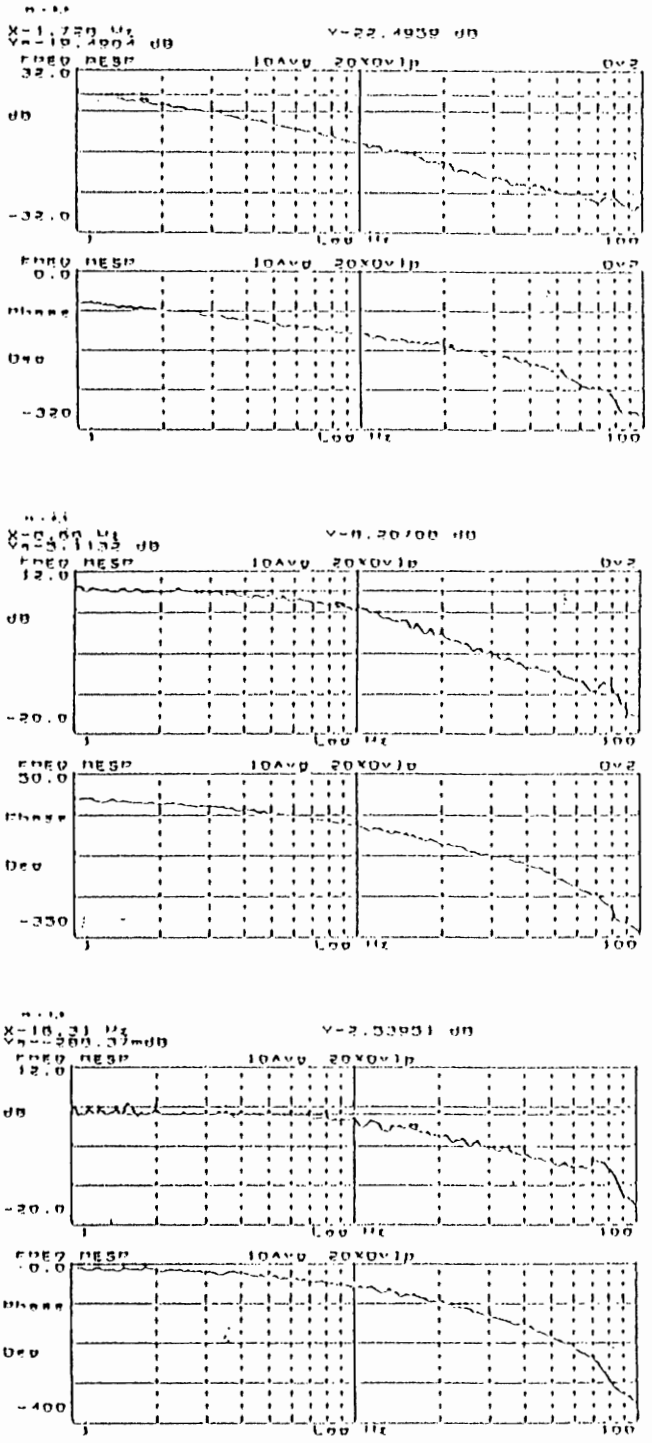

Figure 3.12: Bode plots of the pneumatic force control system for K_{fb} equal to 0.0, 0.5 and 1.0.

Chapter 4

Controlling the Manipulator

4.1 Stiffness Control

Controlling the stiffness of the end effector platform is accomplished by measuring the link displacement and commanding desired forces which are functions of the measured displacement. It has been shown in Chapter 2 that the joint stiffness parameters for a desired end-effector stiffness can be calculated in the home position. The control for each link can be defined easily.

$$\begin{Bmatrix} Output_1 \\ Output_2 \\ Output_3 \end{Bmatrix} = \begin{bmatrix} k_{11} & k_{12} & k_{13} \\ k_{21} & k_{22} & k_{23} \\ k_{31} & k_{32} & k_{33} \end{bmatrix} \begin{Bmatrix} \Delta l_1 \\ \Delta l_2 \\ \Delta l_3 \end{Bmatrix} \tag{4.1}$$

A load sensor fixed to a heavy base was used to check the actual stiffnesses produced by the mechanism. The upper platform was deflected a certain amount and the output force in the **Z** direction was checked. The author found very good correlation between the amount of deflection and the desired output. For example, if the desired $K_Z = 10$ lbs /in and if all three links are deflected a half of an inch, the output force should be 5 lbs in the **Z** direction. The output force varied between 4.9 and 5.1 lbs. The performance of the system greatly increased because of the addition of the inner pressure feedback loop: errors between the measured and desired forces are much smaller than they were previously.

Different stiffness gains are used which allow the mechanism to behave in a desired fashion. The stiffness parameters can be set so that the mechanism behaves like an ankle.

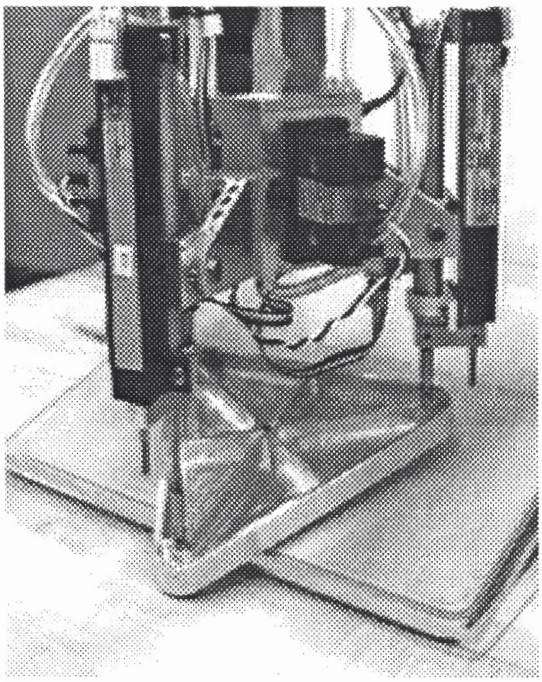

Figure 4.1: Stiffness Control

As stated earlier, the stiffness in the **Z** direction is large while the stifnesses in the θ_X and θ_Y directions are small. This allows for the upper platform to rotate if an object is stepped on, but the force in the **Z** direction still remains vertical and large so that a leg can be effectively supported.

4.2 Impedance Control

Active impedance control for a one degree of freedom link is presented. Because there is very little coupling between the links, each link is assumed to be independent. Also, the dynamics of each link arise from the stiction of the actuators, and the compliance of the air.

The impedance of each link can be defined in terms of the mass, damping, and stiffness parameters as well as the input and external forces.

$$m_a\ddot{x} + d_a\dot{x} + k_a(x - x_d) = f_{in} + F_{ext} \tag{4.2}$$

where m_a, d_a, k_a are the actual mass, damping, and stiffness parameters of the link respectively, f_{in} is the input force, and F_{ext} is an external force applied to the link.

The system's desired impedance behavior is defined according to the following second order differential equation.

$$m_d\ddot{x} + d_d\dot{x} + k_d(x - x_d) = F_{ext} \tag{4.3}$$

To obtained the desired impedance, the input force is defined to be the following.

$$f_{in} = (m_a - m_d)\ddot{x} + (d_a - d_d)\dot{x} + (k_a - k_d)(x - x_d) \tag{4.4}$$

It is customary [39] to substitute an expression for $\ddot{x}$ in terms of the external force into Equation 4.4, but because an external force sensor was not available, the substitution could not be made. $\ddot{x}$ is estimated from the position data instead.

The actual mass, damping, and stiffness parameters are calculated experimentally. An input force is applied to the link, and the position output is recorded. The actual mass term is very low because the upper platform weighs very little. The damping parameter is dominant because of the friction of the seals.

m_a	d_a	k_a
0.00827 lb s^2 /in	0.37 lb s /in	0 lb /in

Because the stiction is prevalent in the system, it is also included in the model. Static friction force is estimated to 0.6 lbs; however, once motion starts, the dynamic friction is approximately 0.3 lbs. The SIMULAB model for the system is in Figure 4.2.

From Equation 4.3, the desired damping ratio and the desired natural frequency can be determined.

$$w_n = \sqrt{\frac{K_d}{m_d}} \tag{4.5}$$

$$\zeta = \frac{D_d}{2\sqrt{K_d m_d}} \tag{4.6}$$

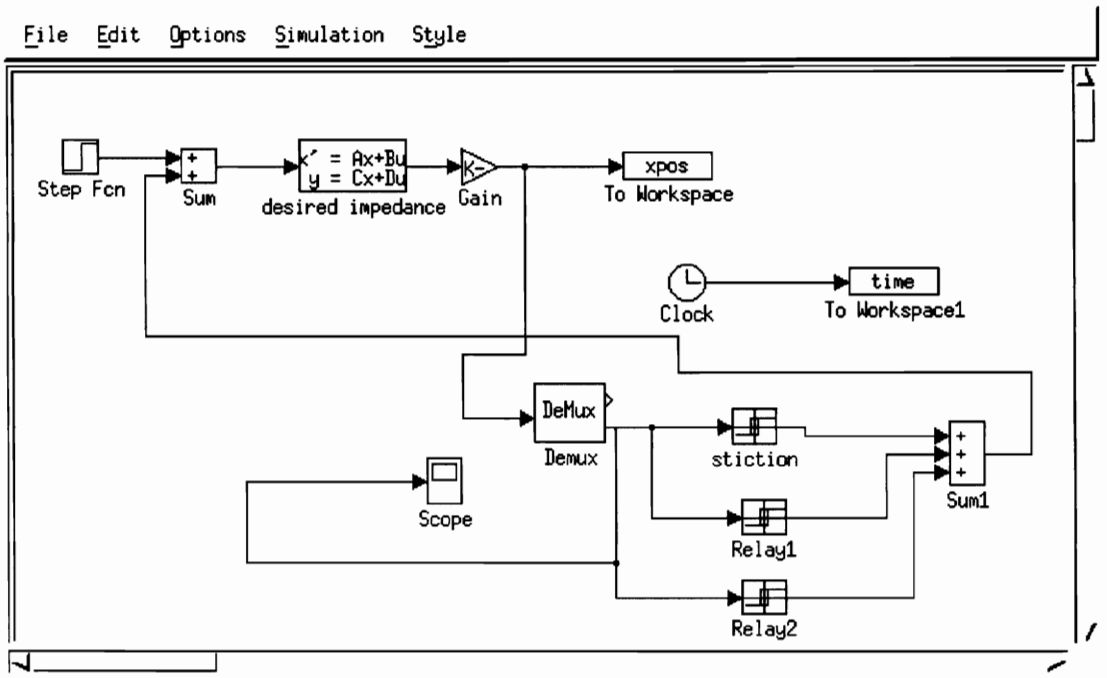

Figure 4.2: Model for Impedance Control

Different values for ζ and w_n were chosen. The values for w_n are kept small because the bandwidth for the system is approximately 70 rad /s. Experimental results were obtained by releasing the manipulator from a position in which one link is 0.5 inches away from the desired position. Velocity and acceleration data were obtained by differentiating the position signal and these signals were filtered to eliminate high frequency noise. A digital filter was used which filtered all frequencies higher than 100 rad /s. In each figure, the dashed line corresponds to the experimental data while the solid line corresponds to the model. The experimental data and the model seem to agree as far as the transient response is concerned. The steady state error is attributed to friction. Even though friction was modeled, it is very hard to determine the actual value. Additional problems with the model could be due to two nonlinearities. One problem is that the actual area on both sides of the double acting piston is different. Friction also becomes larger as the pressure increases because the seals are forced against the sides of the piston. Neither of these nonlinearities were modeled.

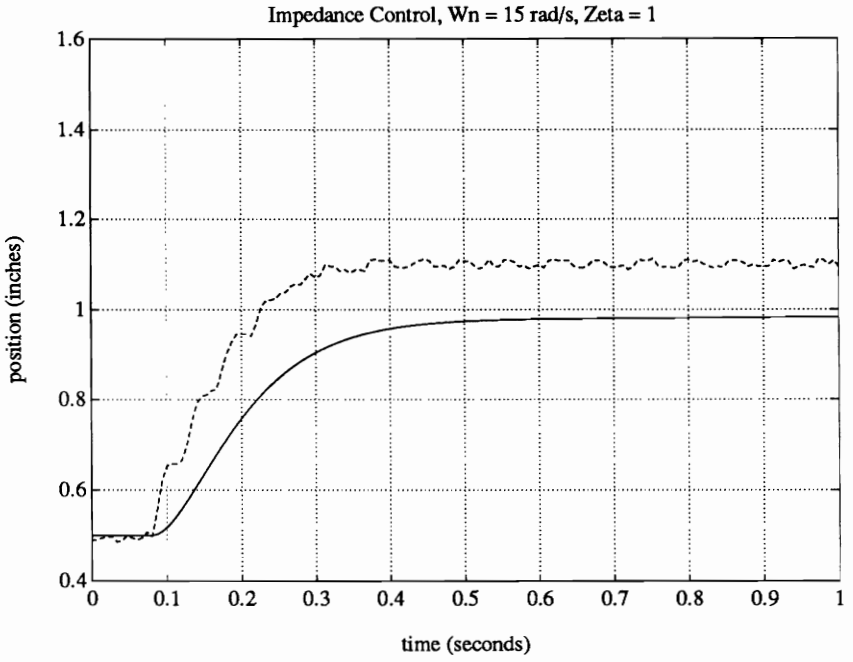

Figure 4.3: Experimental Results for Impedance Control

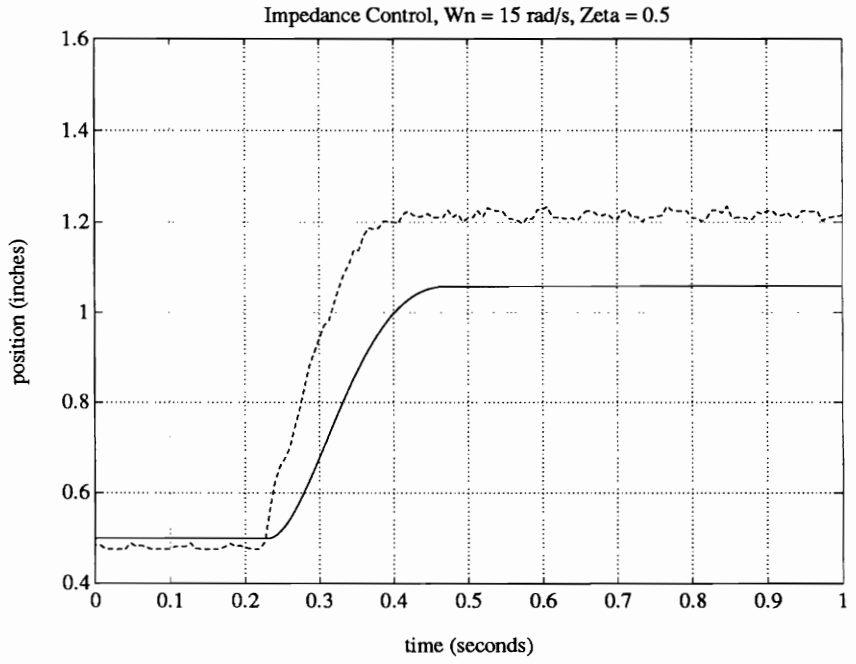

Figure 4.4: Experimental Results for Impedance Control

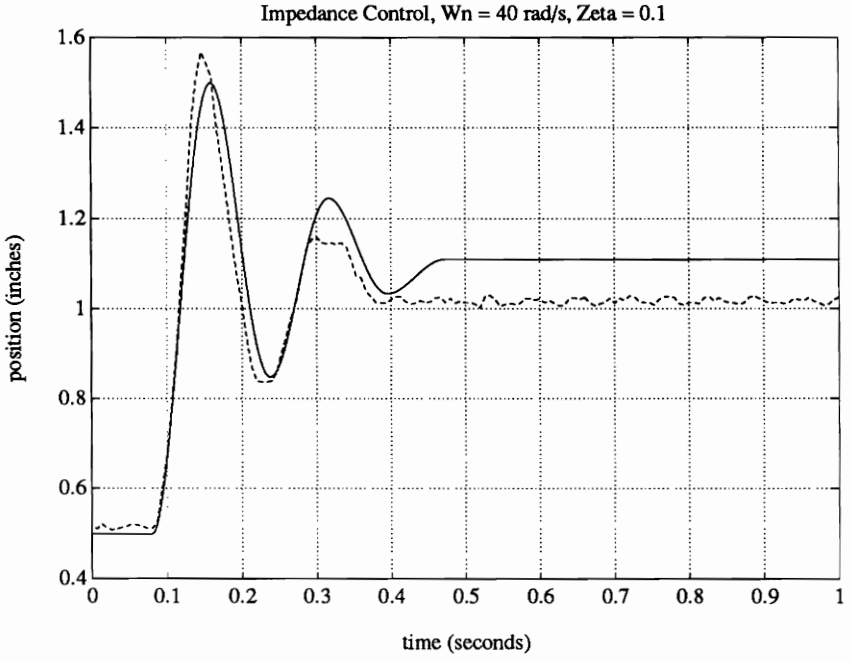

Figure 4.5: Experimental Results for Impedance Control

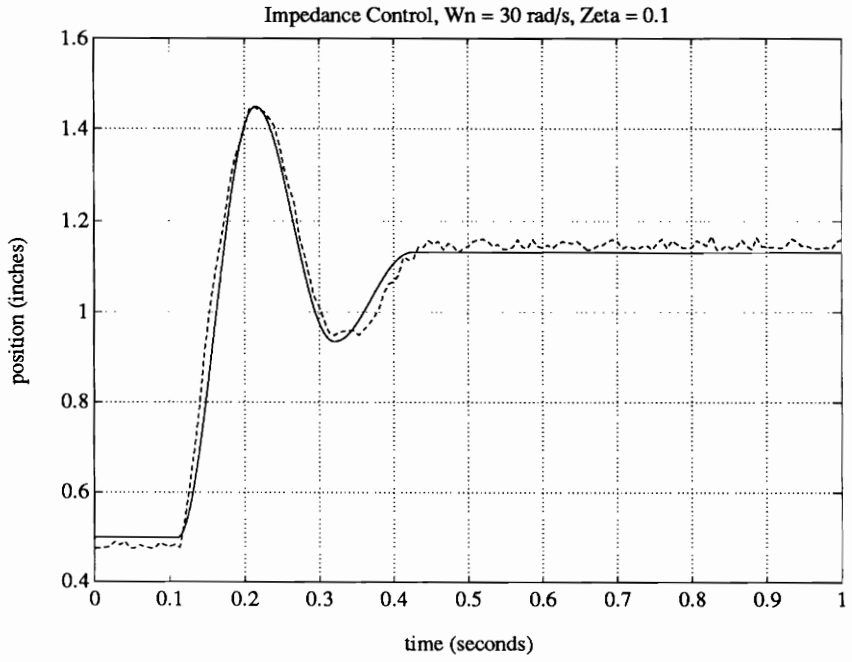

Figure 4.6: Experimental Results for Impedance Control

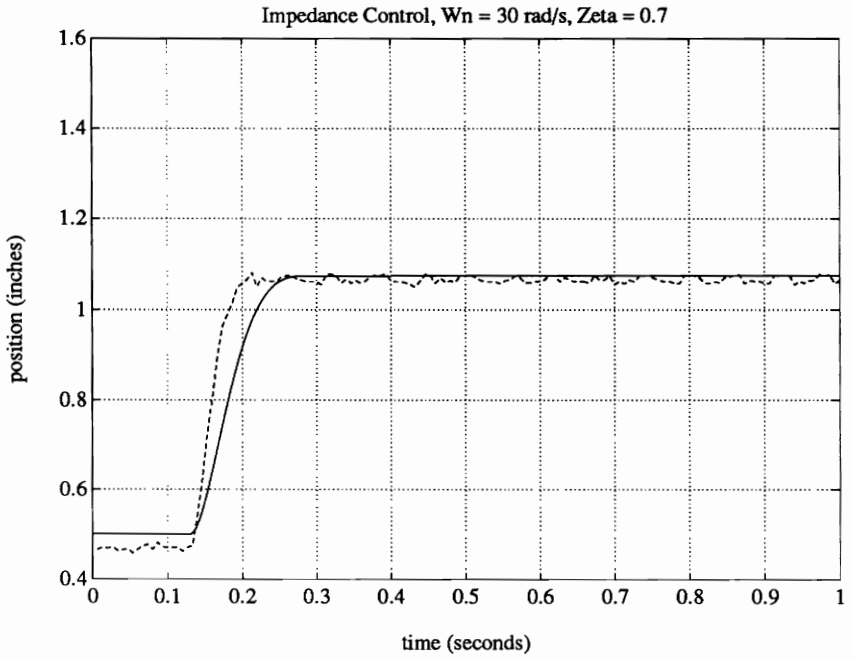

Figure 4.7: Experimental Results for Impedance Control

4.3 Force Control

The tripod manipulator offers a unique solution to the problem of controlling the forces perpendicular to a surface. An arm attached to the mechanism can position it while the mechanism itself could apply the force.

To apply the force, a control law is written for each link. A simple proportional and integral control law is written. The law is based on the recursive trapezoidal rule.

$$error = (F_{des} - F_{act}) \tag{4.7}$$

$$f_{in} = f_{in-1} + K_p(error - errorold) + K_I(error + errorold) \tag{4.8}$$

$$\tag{4.9}$$

The actual force data is calculated by multiplying the pressure times the area. Even though a proportional law is implemented on the computer, the inner pressure feedback loop is still used. The inner pressure loop helps to linearize the relationship between the input voltage and the pressure signal. As stated, before, the performance of the system

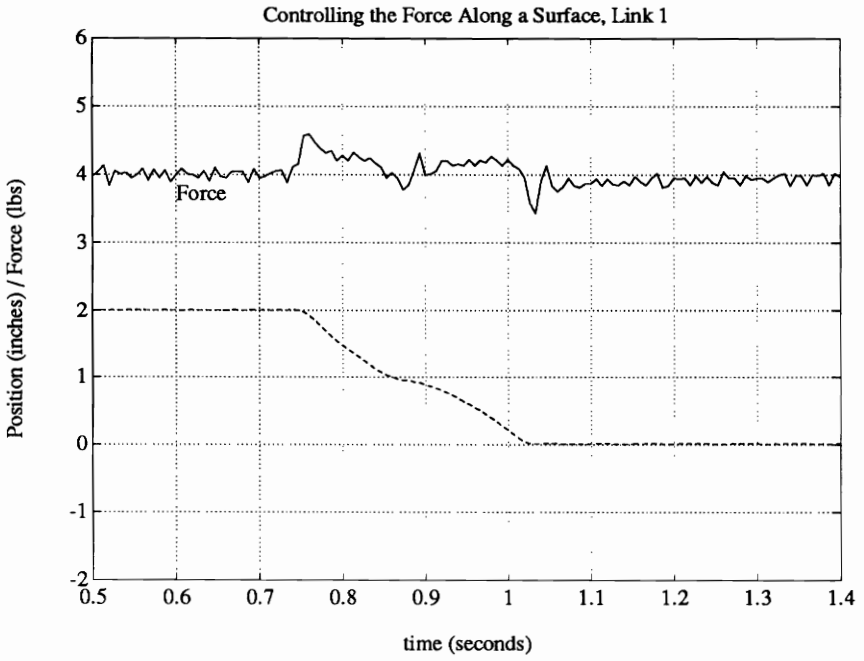

Figure 4.8: Experimental Results for Force Control

increases with the addition of the feedback loop. The integral gain eliminates the steady state error as well as introduces causality into the system. The mechanism can then control the force dynamically.

The mechanism is attached to a two link arm mounted to a mobile platform. The results are shown in Figures 4.8, 4.9, and 4.10. First the arm moves the mechanism over a flat surface and the force is commanded to remain constant at 4 lbs. The arm then moves along an irregular surface where the position of each link changes, but the force still remains relatively constant. This is seen in the Figures 4.8, 4.9, and 4.10. The system is shown in Figure 4.11.

Controlling the force perpendicular to an arbitrary surface is very easy, because the arm can position the mechanism without having to align the platform with the surface since the tripod manipulator both aligns with the surface and applies the desired force. Thus the hybrid force control problem of positioning and controlling the force with a serial mechanism is *naturally* decoupled. The control law for the mechanism controls the force dynamically and is therefore quite robust.

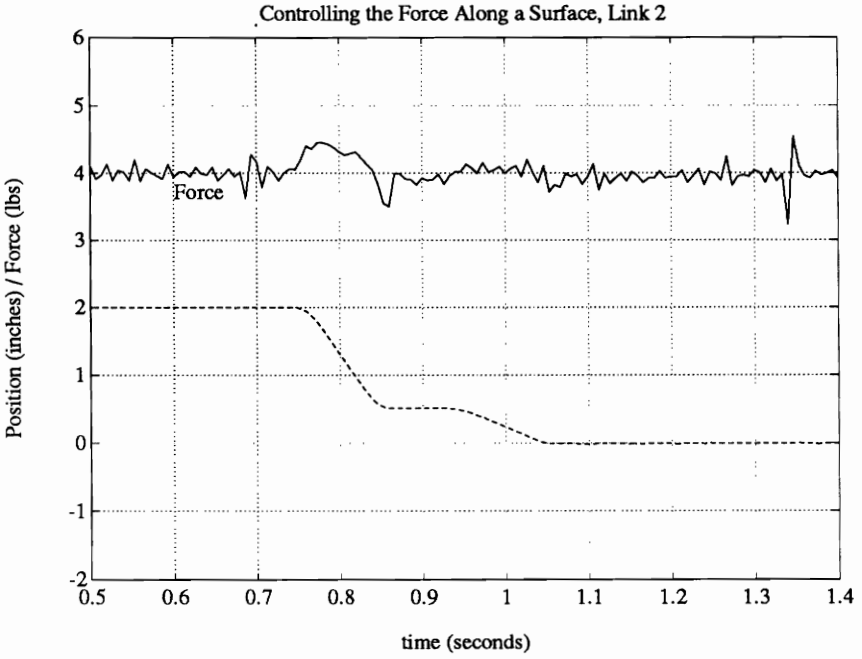

Figure 4.9: Experimental Results for Force Control

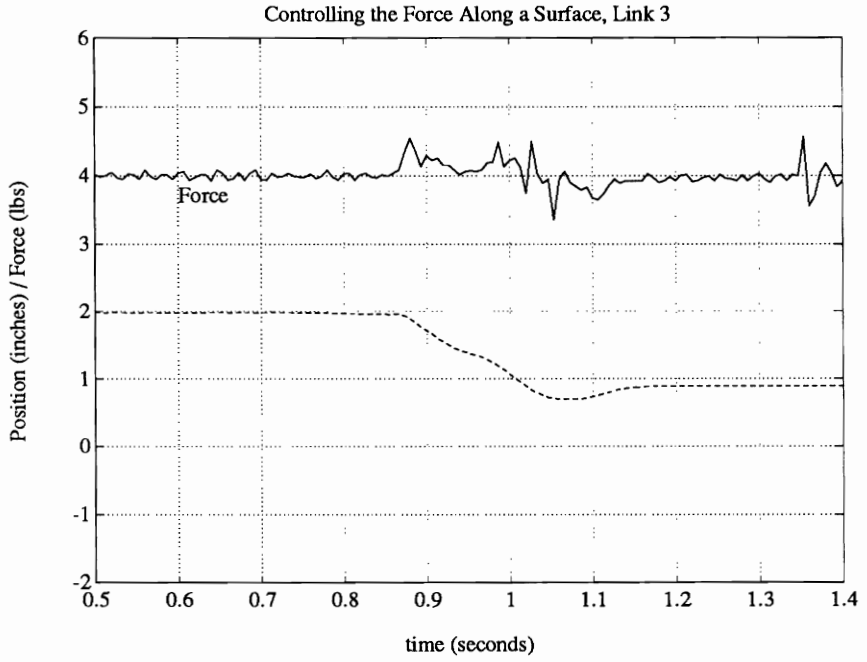

Figure 4.10: Experimental Results for Force Control

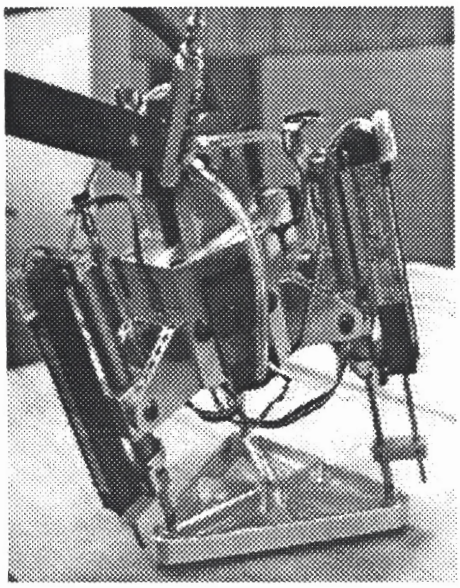

Figure 4.11: Experiments in Force Control

Some assumptions are made for controlling the force of the whole upper platform. Each link has a separate control law which outputs a desired force. The control law does not take into account the tilt of the platform, because the force direction of the resultant vector is almost the same as the **Z** axis even with large rotations of the upper platform. The upper platform can be at an extreme position such as a rotation of $\phi = 22.2$ degrees and the angles θ_i corresponding to the links are still 90, 90, 85.53 degrees. (l1 = l2 = 5 inches l3 = 3 inches)

The force normal to the surface in this case would be: $F_n = (F_1 + F_2 + F_3)\cos 22.2$. The error corresponding to the normal force would be less than 8 percent. The force component along the surface is resisted by the structure of the platform.

Ideally, the tripod mechanism structure would be positioned quite accurately, and the upper platform would rotate very little to account for small errors in orientation. The advantage of the tripod manipulator is that it controls the interaction forces and moments very easily. As described above, the decoupling results in a very simple control law.

Chapter 5

Possible Applications of the Manipulator

5.1 Peg Insertion

Whitney describes a passive mechanical device which is able to insert a rigid peg into a rigid hole [36]. His remote compliant center, (RCC) is able to mechanically insert a peg because of its well designed compliant characteristics. The advantage of the compliance center is that it can insert a peg without using complicated control algorithms. The disadvantage of the RCC is that it is designed to insert pegs of certain sizes. He shows that larger pegs can be used but the insertion force increases and problems with two-point jamming can occur. Following his work, a new passive device incorporating the tripod mechanism will be discussed which uses passive compliance to insert the peg, but can be configured for different sized pegs. The tripod mechanism can also change the stiffness parameters if so desired.

The derivation follows from Whitney's work. A rigid peg supported by a compliance center is shown in Figure 5.1. For one point contact:

$$\sum F_x = 0 = f_n - K_x u + \frac{M_c}{L_g} \tag{5.1}$$

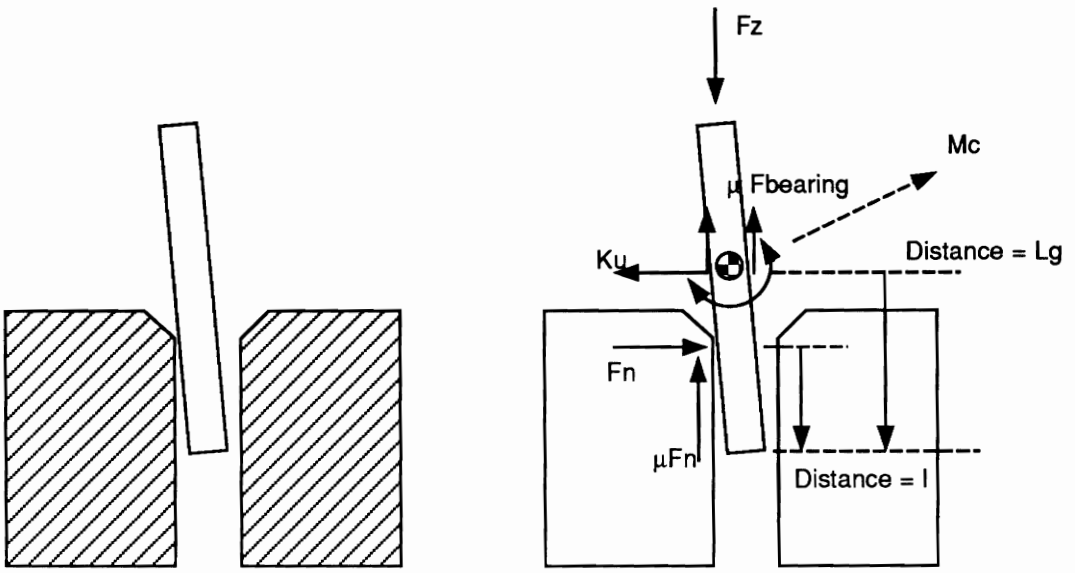

Figure 5.1: Peg Insertion Parameters

$$\sum F_y = 0 = -f_z + 2\mu_2 f_{bearing} + \mu_3 \left(f_n + \frac{M_c}{L_g} \right) \tag{5.2}$$

$$\sum M = 0 = -l f_n - \frac{l M_c}{L_g} - \mu_3 r \left(f_n + \frac{M_c}{L_g} \right) + L_g K_x u - M_c \tag{5.3}$$

$$u = cR + \frac{M_c}{K_x L_g} \tag{5.4}$$

$$c = \frac{R - r}{R} \tag{5.5}$$

$$f_n = K_x c R \tag{5.6}$$

The displacement in the spring, u, is determined by the mating tolerance, c, and the additional term results from the user defined moment, M_c. The goal is to solve for a certain length L_g which will solve the static equations and result in a one point contact. Whitney shows that one point contacts are desirable because the insertion forces are smaller and the possibility of jamming that arises with two point contact is eliminated. It follows from the sum of the forces and moments that:

$$f_z = 2\mu_2 f_{bearing} + \mu_3 \left(f_n + \frac{M_c}{L_g} \right) \tag{5.7}$$

$$L_g = \frac{1}{2}(l + \mu_3 r) + \frac{1}{2}\sqrt{l + \mu_3 r}\sqrt{l + \mu_3 r + H} \tag{5.8}$$

$$H = \frac{4M_c}{K_x c R} \tag{5.9}$$

If L_g is smaller than the value described, the peg will rotate clockwise. If L_g is larger than the value described, the peg will rotate counter clockwise and result in two point contact.

If the peg rotates clockwise it will make a one point contact at the tip. A lower bound on L_g can be described; L_g must be larger than the value described below.

$$L_g = \frac{1}{2}(\mu_3 r) + \frac{1}{2}\sqrt{\mu_3 r}\sqrt{\mu_3 r + H} \tag{5.10}$$

$$H = \frac{4M_c}{K_x c R} \tag{5.11}$$

Further decreasing the length of L_g results in a two point contact with the peg positioned in the opposite orientation. Whitney does not consider M_c and describes a remote compliant center fixed at the tip of the peg where $L_g = \mu r$. As the peg is inserted into the hole, the remote compliant center descends into the hole as well. The problem with the RCC is that the compliance center is built for one sized pegs which satisfies the second equation for L_g. If a peg is larger than the length L_g which is built into the RCC, one point contact will not result.

A system can be built where the compliant center is fixed in space and the first equation for L_g is always satisfied. This is shown in Figures 5.2, 5.3, and 5.4.

The tripod mechanism would position the compliant center above the hole a distance described by:

$$L_g = \frac{1}{2}(\mu_3 r) + \frac{1}{2}\sqrt{\mu_3 r}\sqrt{\mu_3 r + H} \tag{5.12}$$

$$H = \frac{4M_c}{K_x c R} \tag{5.13}$$

K_{theta} would be obtained from the compliance of the air, while K_x would be obtained from attaching a spring system to the platform. Friction wheels would be attached to the spring

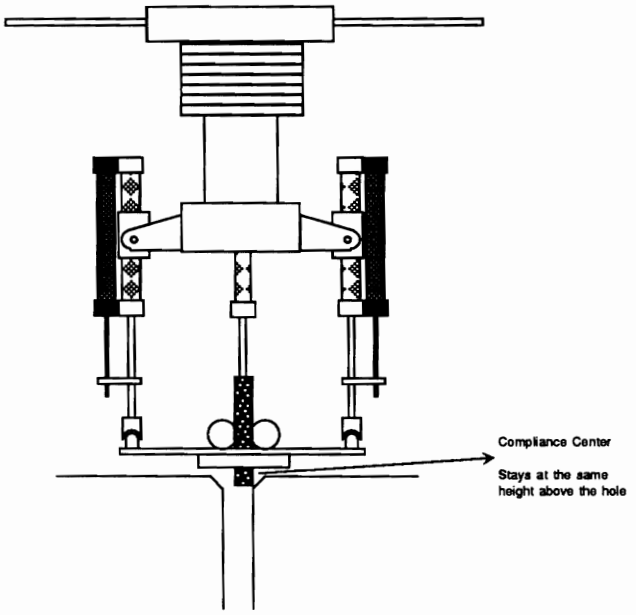

Figure 5.2: Peg Insertion System

system to supply the downward force. The key advantage of this design is that a peg with any length and diameter could be inserted. The initial height would be adjusted for different diameters and M_c could be increased to allow the initial height to be increased. The disadvantage of increasing M_c is that the insertion force would also increase. As the peg is inserted, the length, l, increases and the first equation is still always satisfied because L_g increases as l increases.

In Figure 5.2, the compliance center is positioned at its initial height above the hole. The compliance center is incorporated by the tripod mechanism and its height is not varied. In Figure 5.3, the downward force created by the friction wheels inserts the peg into the hole. As the peg is being inserted, the correct lateral forces and moments are applied by the passive compliance of the tripod mechanism. As shown in Figure 5.4, the peg can also be inserted at an angle because the upper platform can align itself with the surface.

Different possible configurations for the device are shown in Figures 5.2, 5.3, and 5.4.

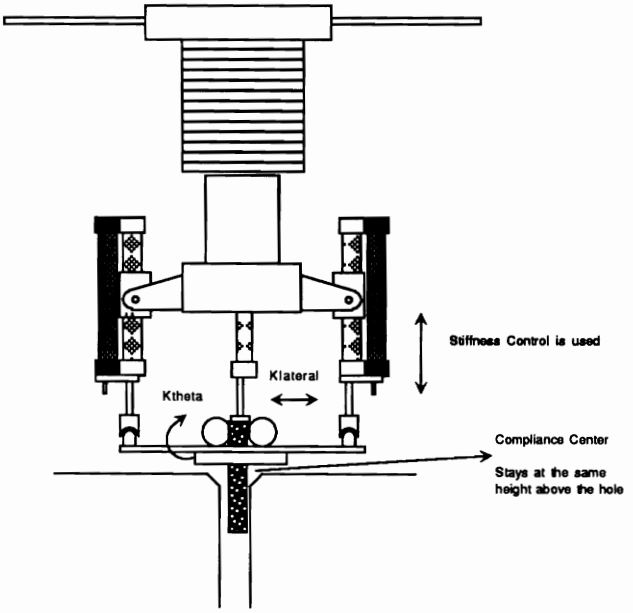

Figure 5.3: Inserting a Peg

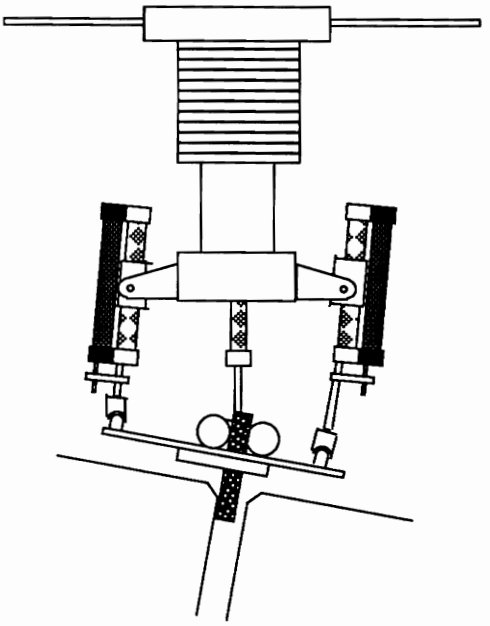

Figure 5.4: Inserting a Peg at an Angle

5.2 Forces Perpendicular to a Surface

The tripod mechanism offers a distinct advantage when controlling the force. Because of the direct drive actuators, the force control bandwidth is reasonably high (approximately 10 Hz). For the tripod mechanism currently built, the bandwidth is lower than the high performance testbed described in Chapter 3 because of the stiction in the cylinders and the large transmission lengths [25]. As shown, the impedance of the system can be controlled; thus the mechanism can be used as an active compliant wrist. An arm could position the mechanism while the mechanism itself can control for any force disturbances.

5.3 Unstructured Environments

In an unstructured environment, unknown forces and disturbances could act on the end effector. The tripod manipulator is able to withstand large impacts. In an experiment designed to simulate impacts, the mechanism was attached to the mobile platform. The two link arm was raised and lowered and the tripod mechanism was forced to strike the ground. The impedance of the mechanism was changed so that wrist's response to the impacts varied. The results showed that the platform was able to absorb the impact very well when the damping parameter was increased.

The mechanism could also be used as an ankle in an unstructured environment. The stiffness parameters could be set so that the stiffness in the vertical direction is large. The ankle could then be forced on for example a rocky terrain and still apply a given stiffness in the **Z** axis.

Chapter 6

Conclusions and Recommendations

6.1 Conclusions

In summary, the important contributions in this thesis are:

- The kinematics of the tripod mechanism are discussed in detail with the purpose of deriving the stiffness matrix. The stiffness matrix at different configurations is shown to be very similar to the matrix for the home position.
- The approach to force control with an acausal model is shown to be fraught with perils. At the very least it is necessary to include an integrator in the control law. Further, the effect of discretization must be thoroughly investigated. The dynamics of the system are shown to be a strong function of the implementation of the control law.
- An inner pressure feedback loop is shown to greatly increase the performance of pneumatic force control.
- Through experiments, force, impedance, and stiffness control are demonstrated.
- Possible applications of the mechanism including its use as an ankle or a wrist are demonstrated. Because of the intrinsic compliance of pneumatics, the mechanism

could also be used in an unstructured environment or as a device for peg insertion.

6.2 Recommendations and Future Work

- In the high-performance testbed described in Chapter 3, the performance is increased for three reasons. The flow control valve's force control bandwidth is much greater than the pressure control valve. The transmission lengths are very short and graphite glass actuators are used. Any pneumatic design should include these characteristics. The tripod mechanism could be redesigned and built with the above design parameters.

- Secondly, a force / torque sensor could be added to the wrist so that a better understanding of the forces exerted at the base of the platform will result.

- In order to explore the proposed decoupled hybrid control scheme it is necessary to provide an additional three degrees of freedom. It is suggested that the parallel manipulator described in Reference [11] would be appropriate.

Appendix A

Appendix: Description of Experimental System

The single-degree-of-freedom pneumatic system consists of three major components, the valve/actuator mechanism, the computer and the amplifier.

The valve/actuator system was designed with off-shelf-components and is shown in Figure A.1.

A flow control valve, Atchley 204, is used to control the flow of air and is the large cylinder in the top portion of the middle of the picture. This valve adjusts the flow of air for a given voltage (If a zero voltage is commanded, the flow of air is stopped). The spool type valve consists of a flapper whose position is adjusted by a torque motor. The torque motor is controlled by an amplifier, which converts a signal of plus or minus ten volts to plus or minus ten milliamperes of current. The amplifier board also has an analog feedback loop which is needed for pressure feedback. Without pressure feedback, the static force-voltage calibration curve is very steep thus making force control virtually impossible. Pressure feedback is accomplished by two pressure transducers, SenSym 1620A, which are mounted at the inlet to the actuators. With the feedback, the force-voltage curve is flatter and quite linear. The valve to actuator distance is minimized by mounting the valve close to the actuators. This reduces the intermediate volume of air which in turn minimizes delays in the transmission line. and improves the performance of the system.

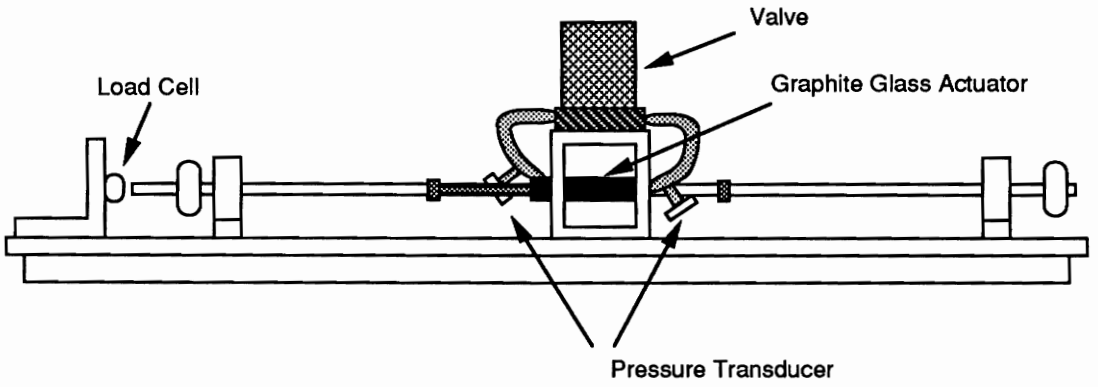

Figure A.1: Schematic for High Performance Testbed

The force feedback is accomplished by a load cell which is located on the bracket at the left of the picture. The large shaft pushes against the load cell resulting in a strain signal which is converted to pounds using a calibration gain. The load cell was rated from zero to two hundred and fifty pounds and the noise of the load cell was plus or minus 0.3 lbs.

Data acquisition is done with an AT-computer using a data acquisition board. The data acquisition board is used to send a voltage signal to the amplifier which controls the valve and it is used to read the voltage from the load cell. The control program is written in C and uses interrupts to achieve real time control.

A.1 Circuit Diagrams for High Performance Testbed

The circuit diagram for the flow control valve is shown in Figure A.2. The gains, span; feedback gain; error gain; and current limiter, can be user adjusted. The computer input to the system can vary between plus and minus ten volts and the pressure difference from the two pressure transducers is used as the feedback.

The circuit diagram for the load cell is shown in Figure A.3. The voltage difference from the load cell is very small because its maximum capacity is two hundred fifty pounds while the maximum load from the testbed is only thirty pounds. Large gains and filters were used so that the signal ranged from zero to ten volts when a zero to twenty pound force was applied.

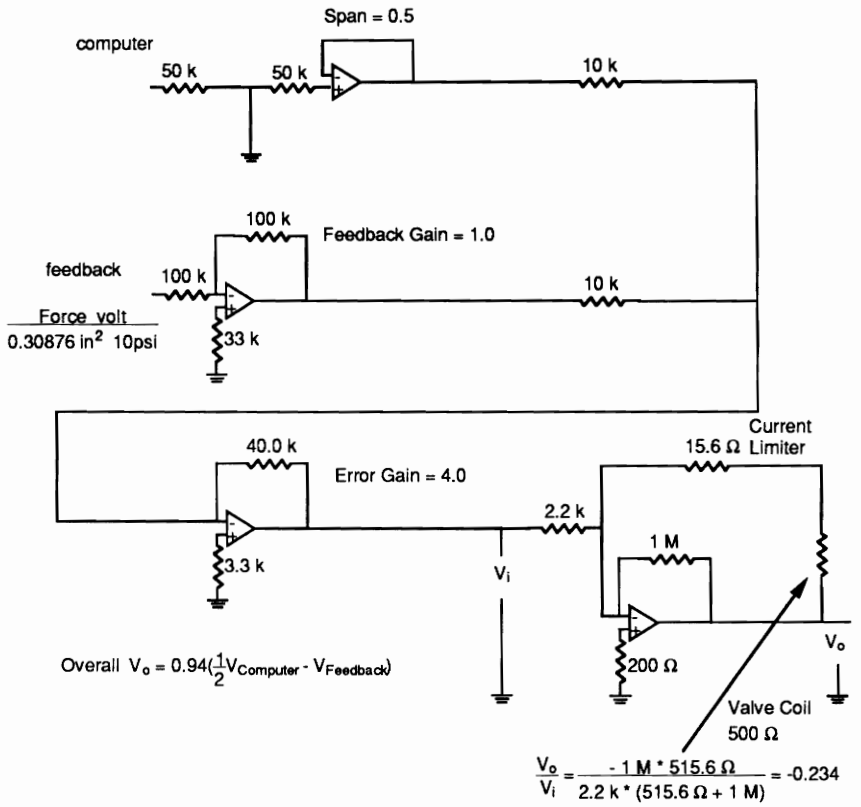

Figure A.2: Circuit Diagram for Flow Control Vale

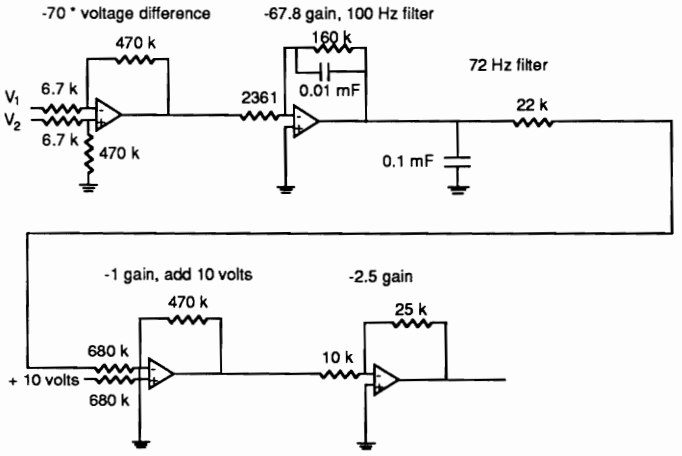

Figure A.3: Circuit Diagram for Load Cell

Bibliography

[1] J.E. Bobrow and S. Liu. An analysis of a pneumatic servo system and its application to a computer-controlled robot. *ASME Journal of Dynamic Systems, Measurement, and Control*, 110():228–235, September 1988.

[2] L. Cai and A.A. Goldenberg. An approach to force and position control of robot manipulators. In *Proceedings of 1990 International Conference on Robotics and Automation*, pages 86–91, Cincinnati, OH, May 1990.

[3] A. Cole, J. Hauser, and S. Sastry. Kinematics and control of multifingered hands with rolling contact. In *Proceedings of 1988 International Conference on Robotics and Automation*, pages 228–233, Philadelphia, PA, April 1988.

[4] E. Colgate and N. Hogan. The interaction of robots with passive environments: applications to force feedback control. In *Advanced Robotics 1989, Proceedings of the Fourth International Conference on International Robotics*, pages 465–474, Columbus, Ohio, June 1989.

[5] N. Hogan. Impedance control: an approach to manipulation: part I. *Transactions of ASME, Journal of Dyamic Systems, Measurement, and Control*, 107(1):1–7, March 1985.

[6] H. Inoue. Computer controlled bilateral manipulator. *Bulletin, Japan Soc. Mech. Eng.*, 1971.

[7] H. Kazerooni. On the robot compliant motion control. *Transactions of ASME, Journal of Dynamic Systems, Measurement, and Control*, 111(3), September 1989.

[8] J. Kerr and B. Roth. Analysis of multifingered hands. *Int. J. of Robotics Research*, 4(4), 1986.

[9] O. Khatib. A unified approach for motion and force control of robot manipulator: the operational space formulation. *IEEE Journal of Robotics and Automation*, RA-3(1):43–53, February 1987.

[10] A.J. Koivo and G. A. Bekey. Report of workshop on coordinated multiple robot manipulators: planning, control, and application. *IEEE Journal of Robotics and Automation*, 4(1):91–93, February 1988.

[11] V. Kumar, B.P. Meyer, and N. Ulrich. Mechanics and design of a planer parallel manipulator. *First National Conference on Applied Mechanisms and Robotics*, November 1989.

[12] V. Kumar, E. Paljug X. Yun, and N. Sarkar. Control of contact conditions for manipulation with multiple robotic systems. In *Proceedings of IEEE International Conference on Robotics and Automation*, May 1991.

[13] K. Lee and D.K. Shah. Dynamic analysis of a three-degrees-of-freedom in-parallel actuated manipulator. *IEEE Journal of Robotics and Automation*, 4(3):361–367, June 1988.

[14] K. Lee and D.K. Shah. Kinematic analysis of a three-degrees-of-freedom in-parallel actuated manipulator. *IEEE Journal of Robotics and Automation*, 4(3):345–350, June 1988.

[15] Z. Li and S. Sastry. Task oriented optimal grasping by multifingered robot hands. *IEEE Transactions of Robotics and Automation*, 4(1), February 1988.

[16] J.J. Mannetje. Pneumatic servo design method improves system bandwidth twenty fold. *Control Engineering*, 79–83, June 1981.

[17] N.H. McClamroch. Singular systems of differential equations as dynamic models for constrained dynamic systems. In *1986 IEEE International Conference on Robotics and Automation*, San Francisco, CA., April 1986.

[18] J.K. Mills and A.A. Goldenberg. Force and position control of manipulators. *IEEE Transactions on Robotics and Automation*, 5(1), February 1989.

[19] K. Ogata. *Modern Control Engineering.* Prentice Hall, Englewood Cliffs, New Jersey, 1990.

[20] E. Paljug, T. Sugar, V. Kumar, and X. Yun. Important considerations in force control with applications to multi-arm manipulation. In *Submitted to the Proceedings of the IEEE International Conference on Robotics and Automation*, May 1992.

[21] E. Paljug, X. Yun, and V. Kumar. Control of rolling contacts in multiple robotic manipulation. In *Proceedings of the IEEE International Conference on Advanced Robotics*, pages 591–596, Psia, Italy, 1991.

[22] R.P. Paul. *Robot Manipulators: Mathematics, Programming, and Control.* The MIT Press, 1981.

[23] R.P. Paul and B. Shimano. Compliance and control. In *Proceedings of the JACC*, pages 694–699, 1976.

[24] G. Pfreundschuh, V. Kumar, and T. Sugar. Design and control of a 3 dof in-parallel actuated manipulator. In *the Proceedings of the IEEE International Conference on Robotics and Automation*, pages 1659–1665, Sacramento, California, May 1991.

[25] G. H. Pfreundschuh. *The Kinematics, Design, and Control of a Parallel Actuated Manipulator.* Master's thesis, University of Pennsylvania, 1990.

[26] M.E. Pittelkau. Adaptive load-sharing force control for two-arm manipulators. In *Proceedings of 1988 International Conference on Robotics and Automation*, pages 498–503, Philadelphia, PA, April 1988.

[27] M.H. Raibert and J.J. Craig. Hybrid position/force control of manipulators. *Transactions of ASME, Journal of Dynamic Systems, Measurement, and Control*, 103(2):126–133, June 1981.

[28] J.K. Salisbury. Active stiffness control of a manipulator in cartesian coordinates. In *Proceedings of the 19th IEEE Conference on Decision and Control*, December 1980.

[29] K. Salisbury and B. Roth. Kinematics and force analysis of articulate mechanical hands. *ASME Journal of Mechanisms, Transmissions and Automation in Design*, 105:35–41, March 1983.

[30] S.A. Schneider and R.H. Cannon. Object impedance control for cooperative manipulation. In *Proceedings of the IEEE International Conference on Robotics and Automation*, Scottsdale, AZ, May 1989.

[31] T. Sugar. *Modeling and Control of a Electro-Pneumatic Servovalve and Graphite Glass Actuator.* Technical Report, University of Pennslyvania, 1991. GRASP Laboratory.

[32] T. Sugar, V. Kumar, and G. Pfreundschuh. A three degree-of-freedom in-parallel actuated manipulator. In *Accepted for the 9th CISM-IFToMM Symposium on the Theory and Practice of Robot Manipulators*, September 1992.

[33] K.J. Waldron, M. Raghavan, and B. Roth. Kinematics of a hybrid series-parallel manipulator system. *ASME Journal of Dynamic Systems, Measurement, and Control*, 111:211–221, June 1989.

[34] K.J. Waldron, M. Raghavan, and B. Roth. Kinematics of a hybrid series-parallel manipulator system, part i: position kinematics. *Proceedings from Winter Annual Meeting, American Society of Mechanical Engineers*, 127–136, December 1987.

[35] J. Wen and K. Kreutz. Motion and force control for multiple cooperative manipulators. In *Proceedings of the IEEE International Conference on Robotics and Automation*, Scottsdale, AZ, May 1989.

[36] D.E. Whitney. Quasi - static assembly of compliantly supported rigid parts. *ASME Journal of Dynamic Systems, Measurement, and Control*, 104:65–77, March 1982.

[37] Y. Xu and R.P. Paul. On position compensation and force control stability of a robot with a compliant wrist. In *IEEE International Conference on Robotics and Automation*, page , Philadelphia, PA, April 1988.

[38] B. Yi, R. Freeman, and D. Tesar. Open-loop stiffness control of overconstrained mechanisms/robotic linkage systems. In *Proceedings of the IEEE International Conference on Robotics and Automation*, Scottsdale, AZ, May 1989.

[39] T. Yoshikawa. *Foundations of Robotics Analysis and Control.* The MIT Press, 1990.

[40] T. Yoshikawa and K. Nagai. Evaluation and determination of the grasping forces in a multifingered grasp. In *Proceedings of 1988 International Conference on Robotics and Automation*, pages 245–248, Philadelphia, PA, April 1988.

[41] T. Yoshikawa and X. Zheng. Coordinated dynamic hybrid control for multiple robots handling one constrained object. In *Proceedings of 1990 International Conference on Robotics and Automation*, Cincinnati, OH, May 1990.

[42] X. Yun. Coordination of two-arm pushing. In *Proceedings of 1991 International Conference on Robotics and Automation*, Sacramento, CA, April 1991.

[43] X. Yun and V. Kumar. An approach to simultaneous control of trajectory and interaction forces in dual arm configurations. In *Fourth International Conference on Advanced Robotics*, Columbus, Ohio, June 1989.

[44] X. Yun, V. Kumar, and N. Sarkar. Control of multiple arm systems with nonholonomic constraints. In *Submitted to the Proceedings of the IEEE International Conference on Robotics and Automation*, May 1992.

[45] Y. Zheng and J.Y.S. Luh. Optimal load distribution for two industrial robots handling a single object. In *IEEE International Conference on Robotics and Automation*, Philadelphia, PA, April 1988.